

<sup>1</sup>           **The Central Time-of-Flight System for**  
<sup>2</sup>           **CLAS12**

<sup>3</sup>           D.S. Carman<sup>a,1</sup>, G. Asryan<sup>a</sup>, V. Baturin<sup>a</sup>, L. Clark<sup>b</sup>  
<sup>4</sup>           R. De Vita<sup>c</sup> W. Kim<sup>d</sup>, B. Miller<sup>a</sup>, A. Ni<sup>d</sup>, and C. Wiggins<sup>a</sup>

<sup>5</sup>           <sup>a</sup>*Thomas Jefferson National Accelerator Facility, Newport News, VA 23606, USA*

<sup>6</sup>           <sup>b</sup>*University of Glasgow, Glasgow G12 8QQ, United Kingdom*

<sup>7</sup>           <sup>c</sup>*INFN, Sezione di Genova, 16146 Genova, Italy*

<sup>8</sup>           <sup>d</sup>*Kyungpook National University, Daegu 41566, Republic of Korea*

---

<sup>9</sup>           **Abstract**

<sup>10</sup>          The Central Time-of-Flight system for the large-acceptance CLAS12 spectrometer  
<sup>11</sup>         in Hall B at the Thomas Jefferson National Accelerator Facility is described. The  
<sup>12</sup>         system consists of a hermetic barrel of scintillation counters at a radius of 25 cm  
<sup>13</sup>         from the beamline. The wedge-shaped counters are roughly 3.4 cm wide, 3.0 cm  
<sup>14</sup>         thick, and 90 cm long, and span a range of polar angles relative to the center of  
<sup>15</sup>         the nominal target location from roughly 35° to 125°. The counters reside in the  
<sup>16</sup>         5-T field of the CLAS12 superconducting solenoid. The bars are read out via bent  
<sup>17</sup>         light guides 1 m long on the upstream end of the counters and 1.6 m long on the  
<sup>18</sup>         downstream end. The phototubes are shielded by a multi-layer dynamical magnetic  
<sup>19</sup>         shield system to reduce the local fringe fields in the range from 400 G to 1000 G  
<sup>20</sup>         down to the level of 0.2 G at the location of the photocathodes. The average intrinsic  
<sup>21</sup>         time resolution of the counters is 65 ps.

---

<sup>22</sup>          PACS:29.40.Mc

<sup>23</sup>          Keywords: CLAS12, time of flight, plastic scintillator, particle identification

---

<sup>1</sup> Corresponding author. Address: 12000 Jefferson Ave., Newport News, VA; e-mail:  
carman@jlab.org.

## Contents

24	1	Overview of CLAS12	3
25	2	Overview of the CTOF System	4
26	3	Design of the CTOF System	7
27	3.1	Geometry	9
28	3.2	Scintillation Material	10
29	3.3	Light Guides	12
30	3.4	Photomultiplier Tube/Voltage Divider Assemblies	17
31	3.5	Magnetic Shields	21
32	3.6	Assembly	29
33	3.7	Installation	31
34	3.8	Electronics	32
35	4	CTOF Performance	37
36	4.1	Bench Measurements	37
37	4.2	CTOF Beam-Data Calibrations	41
38	4.3	Beam Performance	54
39	5	Summary	57
40		Acknowledgements	58
41		References	59

<sup>42</sup> **1 Overview of CLAS12**

<sup>43</sup> The Thomas Jefferson National Accelerator Facility (JLab) recently completed  
<sup>44</sup> a project to double the maximum energy of its electron accelerator from 6 GeV  
<sup>45</sup> to 12 GeV. The experimental equipment in Hall B forms the large-acceptance  
<sup>46</sup> CLAS12 spectrometer that was designed to operate with beam energies up  
<sup>47</sup> to 11 GeV at a nominal beam-target luminosity of  $1 \times 10^{35} \text{ cm}^{-2}\text{s}^{-1}$  to allow  
<sup>48</sup> for precision measurements of exclusive reactions with polarized beam and  
<sup>49</sup> both unpolarized and polarized targets. This spectrometer is based on two  
<sup>50</sup> superconducting magnets, a solenoid in the central region about the target  
<sup>51</sup> and a toroid at forward angles.

<sup>52</sup> The CLAS12 torus has a six-fold symmetry that divides the forward accep-  
<sup>53</sup> tance in the range from  $5^\circ$  to  $35^\circ$  into six  $60^\circ$ -wide sectors. It produces a  
<sup>54</sup> field primarily in the azimuthal direction. The field strength at its nominal  
<sup>55</sup> full current in terms of  $\int B d\ell$  is 2.8 T at  $5^\circ$  and 0.5 T at  $35^\circ$ . A set of three  
<sup>56</sup> multi-layer drift chambers in each sector (before the field, within the field, and  
<sup>57</sup> after the field) and a forward micromegas vertex tracker are used for charged  
<sup>58</sup> particle tracking to measure momenta. Downstream of the torus each sector  
<sup>59</sup> is instrumented with a Cherenkov counter for  $\pi/K$  separation (five sectors  
<sup>60</sup> are instrumented with low threshold gas Cherenkov counters and one sec-  
<sup>61</sup> tor is instrumented with a ring-imaging Cherenkov counter), a scintillation  
<sup>62</sup> counter wall for charged particle timing measurements, and an electromag-  
<sup>63</sup> netic calorimeter system for electron and neutral particle identification. Just  
<sup>64</sup> upstream of the torus is a large-volume high-threshold gas Cherenkov counter  
<sup>65</sup> for electron identification and a tagging system to detect electrons and photons  
<sup>66</sup> at scattering angles below  $5^\circ$ .

<sup>67</sup> The CLAS12 solenoid spans the central angular range from  $35^\circ$  to  $125^\circ$  and  
<sup>68</sup> has a uniform 5 T central field. The solenoid serves to focus the low-energy  
<sup>69</sup> Møller background down the beam pipe to the beam dump away from the  
<sup>70</sup> acceptance of the spectrometer. The detectors mounted within the solenoid  
<sup>71</sup> include a thick scintillation counter barrel for neutron identification, a barrel  
<sup>72</sup> of thin scintillation counters for charged particle timing measurements called  
<sup>73</sup> the Central Time-of-Flight (CTOF) system, and a set of tracking detectors  
<sup>74</sup> about the target.

<sup>75</sup> Fig. 1 shows a three-dimensional representation of CLAS12 from the design  
<sup>76</sup> model to highlight the layout and the scale of the spectrometer. The CLAS12  
<sup>77</sup> spectrometer was installed and instrumented in Hall B in the period from  
<sup>78</sup> 2012 to 2018. The CLAS12 spectrometer took the place of the original CLAS  
<sup>79</sup> spectrometer [1] that operated in Hall B in the period from 1997 to 2012 when  
<sup>80</sup> it was decommissioned.

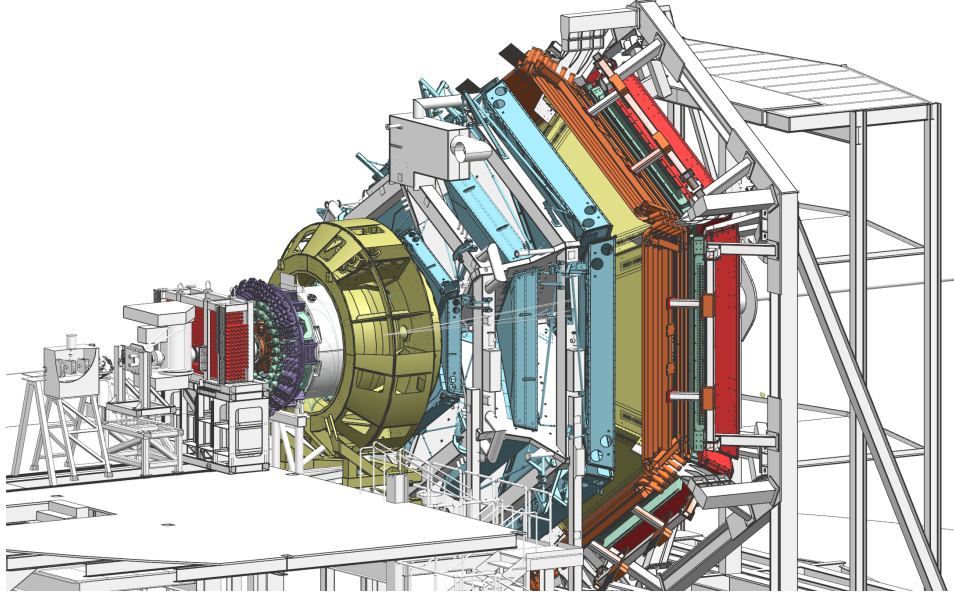


Fig. 1. (Color Online) Model representation of the CLAS12 spectrometer in Hall B at Jefferson Laboratory. The electron beam is incident from the left side of this figure. The CLAS12 detector is roughly 10 m in scale along the beam axis. For further details on the individual subsystems that make up the CLAS12 spectrometer see Ref. [2].

This paper focuses on the CLAS12 CTOF detector system and is organized as follows: Section 2 provides a high-level overview of the CTOF system and its design requirements, Section 3 provides a technical description of the system design, and Section 4 highlights the performance of the system through both bench testing with cosmic rays, as well as during the 2017 beam commissioning run and 2018 data runs. Finally, Section 5 provides a summary regarding the CTOF detector system for CLAS12.

## 2 Overview of the CTOF System

The CTOF system is used to measure the flight time of charged particles emerging from interactions in the target in the angular range from  $35^\circ$  to  $125^\circ$ . The system specifications call for an average time resolution for each counter along its full length of  $\sigma_{TOF}=65$  ps. The CTOF detector surrounds the experimental target at a radial distance of 25 cm and consists of 48 90-cm-long scintillation bars having a trapezoidal cross section to form a hermetic barrel as shown in Fig. 2. The barrel is positioned inside of the CLAS12 5-T superconducting solenoid magnet just inside a set of thick scintillation counters used for neutron detection and just outside of the central tracking system as shown in Fig. 3. This figure shows that the CTOF is mounted to the solenoid with the beamline along the symmetry axis of the CTOF barrel. A summary of the CTOF technical parameters is given in Table 1.

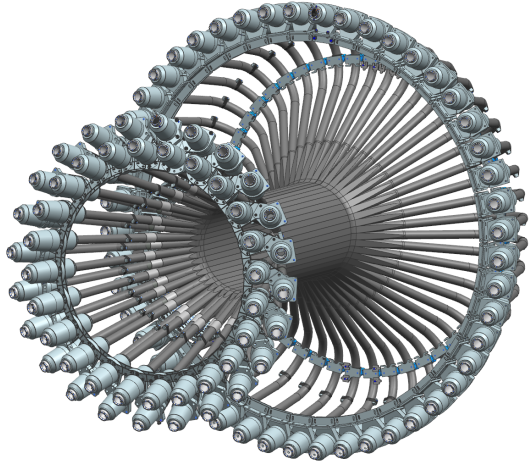


Fig. 2. (Color Online) View of the Central Time-of-Flight (CTOF) system for CLAS12. The scintillation bars form a hermetic barrel and the PMTs are attached to the ends of long light guides attached to each end of the bars. The beam enters the detector in this figure from the left side.

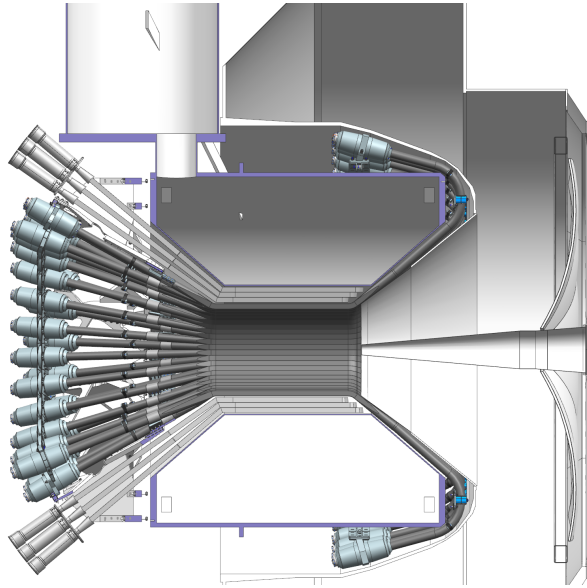


Fig. 3. (Color Online) CTOF mounted within the CLAS12 solenoid in a cut view where the beam axis runs along the CTOF barrel symmetry axis with the beam entering from the left. This figure shows the CTOF counters in relation to the Central Neutron Detector and the cryostat of the superconducting solenoid.

101 Each counter is read out via a photomultiplier tube (PMT) on each end  
 102 through long light guides. As shown in Figs. 2 and 3, the upstream light  
 103 guides are straight and the downstream light guides are bent to curve around  
 104 the downstream face of the solenoid magnet. The upstream light guides are  
 105 1 m long and the downstream light guides are 1.6 m long. These long light  
 106 guides are necessary to position the field-sensitive PMTs in reduced regions of  
 107 the solenoid fringe field. However, even in these positions, the PMTs reside in

108 inhomogeneous fields at levels as large as 1 kG at the location of the upstream  
 109 PMTs and as large as 400 G at the location of the downstream PMTs. In order  
 110 to allow for operation of the PMTs in this environment, they are mounted  
 111 within multi-layer magnetic shields (see Section 3.5).

112 The main requirement for the CTOF system is that its counters provide ex-  
 113 cellent timing resolution for particle identification. Given the nominal timing  
 114 resolution of the counters, the momentum threshold for particle identification  
 115 can be defined. These thresholds are quoted at the  $3\sigma$  level for CTOF, which  
 116 amounts to the momenta where particle identification can occur with up to  
 117 an order of magnitude difference in the relative yields of the different species.  
 118 The timing resolution is illustrated by computing the flight time differences  
 119 between different charged particle species, pions, kaons, and protons, for tracks  
 120 normally incident on the detector. Fig. 4 shows the computed time differences  
 121 as a function of momentum. Where the  $3\sigma$  line crosses the computed time dif-  
 122 ference curves defines the momentum limit for particle identification for each  
 123 particle species. These limits are quoted as 0.58 GeV for  $\pi/K$  separation,  
 124 0.93 GeV for  $K/p$  separation, and 1.14 GeV for  $\pi/p$  separation (see Table 1).  
 125 The minimum momentum acceptance for CTOF is roughly 300 MeV as lower  
 126 momentum tracks are curled up in the solenoid field and never reach the inner  
 127 surface of the CTOF counters.

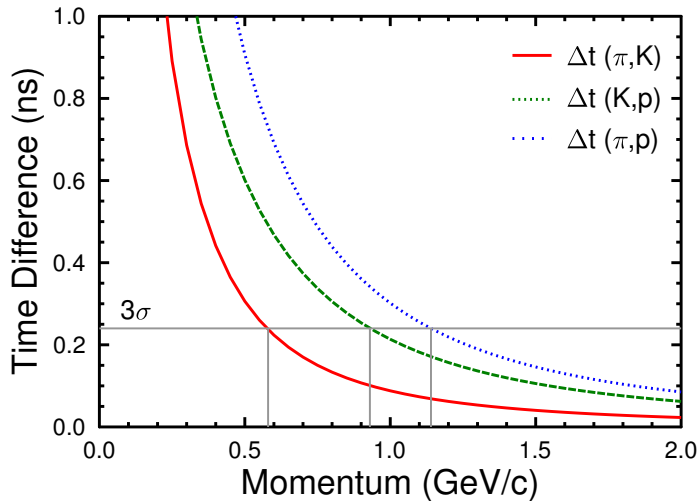


Fig. 4. (Color Online) Plot of time difference between different charged particle species as a function of momentum for normally incident tracks. The momentum at the time difference separation of  $3\sigma$  gives a measure of the particle identification capabilities of the CTOF system. The minimum momentum for tracks to reach the CTOF system is roughly 300 MeV.

128 Fig. 5 shows a plot of the momentum versus polar angle for pions in CLAS12  
 129 from beam data of an 11 GeV electron beam incident on a hydrogen target.  
 130 Here it is seen that the typical track momenta accepted by CTOF are in the  
 131 range below 2 GeV.

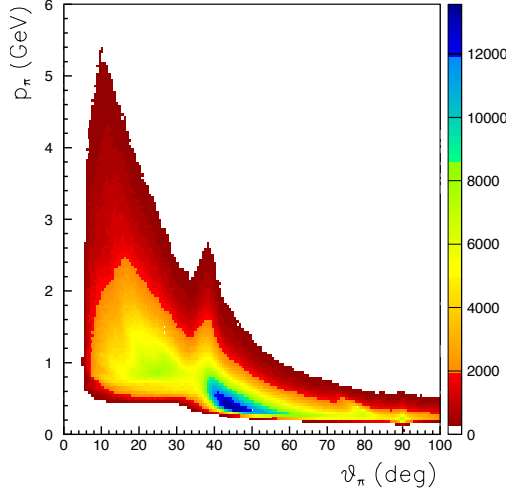


Fig. 5. (Color Online) Plot of momentum vs. polar angle for charged pions in CLAS12 from beam data for a 10.6 GeV electron beam incident upon a liquid-hydrogen target. The discontinuity at  $\theta = 35^\circ$  is due to the small acceptance gap between the Forward and Central Detectors. The typical momentum of charged tracks in the Central Detector is less than 2 GeV.

132 The scintillation counter signals are used in the CLAS12 Level 1 trigger to de-  
 133 fine charged hadrons in the Central Detector, as well as to provide an effective  
 134 charged particle veto for the neutron detector system located radially outward  
 135 of the CTOF. The CTOF system must, therefore, provide signals represent-  
 136 ing a uniform response with adequate granularity to select particles reaching  
 137 the CTOF detectors. The pulse height information from the CTOF system is  
 138 also used for energy-loss measurements to provide supplemental means for the  
 139 identification of slow particles.

140 With the limited radial extent within the 100 cm diameter solenoid, the thick-  
 141 ness of the CTOF scintillation bars was limited to  $\sim 3$  cm. In order to accom-  
 142 modate the target and the central tracking system, the CTOF was positioned  
 143 at a radius from the beamline of 25 cm. To ensure maximal  $\phi$  acceptance, the  
 144 individual CTOF counters have a wedge-shaped geometry to form a hermetic  
 145 barrel. The width of the counters of  $\sim 3.4$  cm was selected to ensure that the  
 146 maximum counting rates did not exceed 500 kHz per counter with the solenoid  
 147 at its nominal full field and a beam-target luminosity of  $1 \times 10^{35} \text{ cm}^{-2}\text{s}^{-1}$ .

### 148 3 Design of the CTOF System

149 The CTOF barrel is composed of 48 wedge-shaped scintillation bars roughly  
 150 90-cm long, read out through 1-m-long (upstream) and 1.6-m-long (down-  
 151 stream) Acrylic light guides attached to the ends of the bars. Extensive ex-  
 152 perience with the design and calibration of the scintillation bars for the CLAS

Parameter	Design Value
Counters	Barrel of 48 EJ-200 bars; double-ended readout
Angular Coverage	$\theta: (35^\circ, 125^\circ)$ , $\phi: (-180^\circ, 180^\circ)$
Counter Dimensions	Trapezoidal cross section $\sim 3.4 \times 3.0 \times 90 \text{ cm}^3$
PMTs	Hamamatsu R2083 (H2431-MOD assembly)
Upstr. Light Guides	O.D.=5.08 cm, 1-m-long, focusing design, straight
Dnstr. Light Guides	O.D.=5.08 cm, 1.6-m-long, focusing design, bent 135°
Magnetic Shields	3 ferromagnetic layers with inner compensation coils
Timing Resolution	65 ps / 80 ps
$\pi/K$ separation	$3\sigma$ up to 0.58 GeV
$K/p$ separation	$3\sigma$ up to 0.93 GeV
$\pi/p$ separation	$3\sigma$ up to 1.14 GeV

Table 1

CTOF technical design parameters.

153 spectrometer (15 cm wide by 5 cm thick) [4] and for the forward angle time-  
 154 of-flight system for CLAS12 (6 cm wide by 6 cm thick) [5], has shown that for  
 155 1-m-long rectangular scintillation counters without light guides, intrinsic av-  
 156 erage timing resolutions in the range from 40 ps to 80 ps can be achieved after  
 157 all corrections are included. For the CTOF design with its roughly 3.4 cm by  
 158 3.0 cm scintillation bars and long light guides, studies of prototype counters  
 159 showed that an average time resolution of  $\sim 65$  ps could be achieved only after  
 160 careful optimization of the overall system design [6].

161 The design timing resolution for the individual CTOF counters includes con-  
 162 tributions intrinsic to the CTOF system itself and contributions from other  
 163 CLAS12 subsystems. The intrinsic resolution is determined mainly by the  
 164 number of photons created in the scintillation bar by passing charged par-  
 165 ticles that ultimately propagate to the photocathodes of the PMTs. Due to  
 166 the geometry of the scintillation bar and the light guides, there are atten-  
 167 uation losses of the created light. As well, the photons that propagate to the  
 168 PMTs are dispersed in time via the different paths that they travel. The re-  
 169 sponse of the PMT, including variations in response across the photocathode,  
 170 causes further dispersion of the times of the created photoelectrons reaching  
 171 the accelerating structure of the PMT. Each of these effects must be folded  
 172 in with the additional signal dispersion as it is produced along the acceler-  
 173 ating structure of the PMT to produce the signal pulse that is used for the  
 174 time measurement. These contributions determine the intrinsic resolution of  
 175 the counter assembly. For our purposes we also include the accounting of the  
 176 intrinsic resolution effects from signal dispersion along the readout signal ca-

bles and the resolution smearing of the readout electronics. These resolutions were determined during our bench test measurements detailed in Section 4.1. However, the overall effective resolution of the system also includes additional smearing effects from other CLAS12 subsystems that are required as input to calibrate the CTOF response. This includes accurate determination of the track path length and reaction vertex point from the central tracking reconstruction, the event start time from the Forward Detector, and the RF time associated with the beam bucket for the event. The overall effective resolution measurements determined during beam studies in CLAS12 are detailed in Section 4.2.6. Table 1 therefore includes two measures of the CTOF design timing resolution. The value of 65 ps is our requirement for the intrinsic timing resolution and 80 ps represents the overall effective resolution that sets the  $3\sigma$  specifications for particle identification.

In this section the design details of the scintillation bars, the light guides, the magnetic shields and the electronics are discussed. Each component of the system design was considered within the context of the design constraints both for the CTOF and the neighboring detector subsystems, and optimized against cost and performance considerations.

### 3.1 Geometry

The scintillation bars of the CTOF barrel are composed of two slightly different designs that alternate in azimuth. A pair of neighboring counters is shown in Fig. 6. The difference between the two designs is in the upstream straight light guide and the upstream end of the scintillation bars where they attach to the light guide. This design feature is necessary to allow for sufficient spacing for the bulky magnetic shields and their associated support structure. The downstream elements of the design are identical for all counters.



Fig. 6. A pair of neighboring CTOF counters with two slightly different designs for the upstream light guide and the upstream end of the scintillation bars.

The two different CTOF counter designs have a slightly different pitch angle for the scintillation bars on the upstream side. The “low-pitch” angle design

205 has a pitch angle of  $21.8^\circ$  and the “high-pitch” angle design has a pitch angle  
 206 of  $29.1^\circ$ . For both the low-pitch and high-pitch angle designs, the scintilla-  
 207 tion bars have a pitch angle at the downstream end of  $36.0^\circ$ . Fig. 7 shows a  
 208 schematic side view and end view of a “generic” scintillation bar.

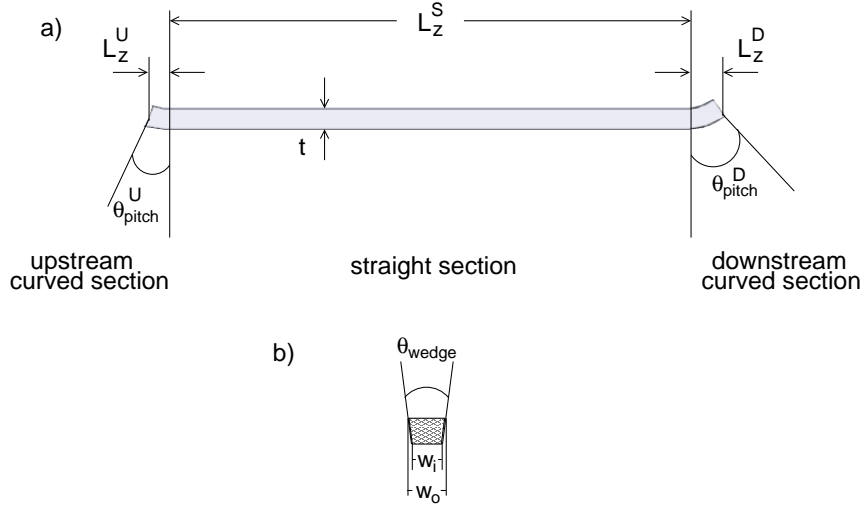


Fig. 7. Schematic views of a generic CTOF scintillation bar showing a) a side view and b) an end view. The parameters used to define the geometry of the bar are listed. See Table 2 for the detailed specifications.

209 The scintillation bar design is essentially a uniform wedge-shaped piece of  
 210 scintillation material that subtends a  $7.5^\circ$  azimuthal range as seen from the  
 211 target. The very ends of the bars curve upwards to join the light guides. A  
 212 simplified description of the two different CTOF scintillation bar designs is  
 213 given in Table 2 using the variables defined in Fig. 7. Here  $L_z$  is the section  
 214 length along the beam/z-axis,  $w_i$  ( $w_o$ ) is the width of the scintillation bar  
 215 at its inside (outside) face, and  $\theta_{wedge}$  is the azimuthal angle subtended by  
 216 each bar as seen from the target. The complete description of the scintillation  
 217 bar geometry for the CTOF is made a bit more complicated by the fact that  
 218 the bars are not a uniform wedge-shaped cross section from end to end. They  
 219 actually have a slightly projective geometry near the ends to match the designs  
 220 of the light guides but they always fit within a  $7.5^\circ$  azimuthal wedge from the  
 221 target. The surface area of the ends of each counter element  $A_{end}$  is listed  
 222 in Table 2. A more complete description of the counter geometry is given in  
 223 Ref. [7].

### 224 3.2 Scintillation Material

225 To optimize the time resolution for the CTOF system, the scintillation bars  
 226 were required to provide a fast time response with low light attenuation. For

Section	Parameter	Design Value	
		Low-Pitch Angle	High-Pitch Angle
Upstream	$L_z^U$	2.924 cm	4.125 cm
	$\theta_{pitch}^U$	21.8°	29.1°
	$A_{end}$	11.20 cm <sup>2</sup>	12.13 cm <sup>2</sup>
Straight	$L_z^S$	80.683 cm	
	$A_{end}$	10.32 cm <sup>2</sup>	
Downstream	$L_z^D$	5.624 cm	
	$\theta_{pitch}^D$	36.0°	
	$A_{end}$	11.02 cm <sup>2</sup>	
Scintillation Bar	$w_i$	3.211 cm	
	$w_o$	3.607 cm	
	$\theta_{wedge}$	7.5°	
	$t$	3.022 cm	

Table 2

Geometry specifications for the CTOF scintillation bars. See Fig. 7 for details on the definitions of the parameters.

this application EJ-200 plastic scintillator from Eljen [8] was selected. This material has the same technical specifications as for BC-408 by Bicron [9]. EJ-200 uses polyvinyltoluene as its base polymer. The characteristics of this material are detailed in Table 3.

Light Output	64% anthracene
Wavelength of Max. Emission	425 nm
Rise Time	0.9 ns
Decay Time	2.1 ns
Pulse Width	2.5 ns (FWHM)
Density	1.023 g/cm <sup>3</sup>
Bulk Attenuation Length	380 cm
Refractive index	1.58

Table 3

The properties of the plastic scintillator EJ-200 used for the CTOF scintillation bars.

The bulk attenuation length of this material is stated by its manufacturer to be  $\sim 4$  m. However, the practical attenuation length of the actual prepared bars is smaller than this bulk value as the path length of photons from the

234 charged particle intersection point to the ends of the bar is increased due  
235 to the finite geometry of the bar. This practical attenuation length should be  
236 longer than the bar to ensure sufficient photon statistics at the ends of the bar.  
237 For the CTOF scintillation bars, the manufacturing specification was that the  
238 bar attenuation length be longer than 280 cm. Measurements of the practical  
239 attenuation length of the CTOF counters, which include the light guides, see  
240 Section 4.2.2 for details, are reduced from this value by a factor of two.

241 The scintillation bars were required to be clear and free of visual inclusions, air  
242 bubbles, and cracks. The bars were machined with diamond-tooled end mills  
243 on two faces and were cast against glass on the other two faces. Upon delivery  
244 the bars were subjected to additional hand polishing to further improve the  
245 surface quality in some cases. The scintillation bar polishing generally followed  
246 the guidelines recommended by Eljen [10]. Using a low-speed random orbital  
247 sander, the surface was sanded using a continuous stream of water across the  
248 sanding head with sandpaper grits from 400 to 6000 in roughly 10 even steps.  
249 The bar was washed after each step with soapy water and then rinsed with  
250 water. Using a soft cotton cloth, a final hand polishing was then performed  
251 using alumina powders with particle sizes of  $1\text{ }\mu\text{m}$ ,  $0.3\text{ }\mu\text{m}$ , and  $0.05\text{ }\mu\text{m}$ , again  
252 with washing and rinsing between each step. Care was taken in all phases of  
253 handling of the bars to wear gloves and to avoid contact with alcohols or other  
254 solvents.

255 *3.3 Light Guides*

256 The locations of the upstream and downstream PMTs for the CTOF system  
257 are tightly constrained by the layout of the CLAS12 Central Detector. On the  
258 upstream end of CTOF, the PMTs must be positioned in locations where the  
259 fringe field from the solenoid is no larger than  $\sim 1\text{ kG}$ , which is the practi-  
260 cal limit of our magnetic shield design. Given the design constraints of the  
261 tracking and target systems located radially inward of the CTOF system and  
262 the neutron detector located radially outward of the CTOF system, as well  
263 as the necessary detector support structures, the upstream light guides for  
264 CTOF were required to be  $\sim 1\text{ m}$  long and project away from the beamline  
265 in the angular range from  $20^\circ$  to  $30^\circ$ . On the downstream end of CTOF, the  
266 design of the high-threshold Cherenkov detector system requires it to be po-  
267 sitioned very close to the downstream face of the solenoid. This required the  
268 downstream CTOF PMTs to be placed on the outer surface of the solenoid  
269 magnet, which required that the downstream CTOF light guides curl around  
270 the downstream end of the solenoid with a minimum length of  $\sim 1.6\text{ m}$ . For  
271 both the upstream and downstream light guides, the overall design principle  
272 was to ensure that the light guides were as short as possible to optimize the  
273 light transmittance and thus optimize the counter timing resolution.

274 The constraints on the light guides required that they match the wedge-shaped  
 275 cross section of the scintillation bar at one end and match the circular shape  
 276 of the PMT at the other end, while being restricted to lie fully within the  $7.5^\circ$   
 277 azimuthal allotment for each of the 48 counters. The CTOF light guides were  
 278 manufactured by Plastic-Craft [11] from 5.08-cm diameter cast Acrylic rods  
 279 ( $n=1.49$ ). The downstream light guides were cast as straight rods and bent on  
 280 a forming mandrel after heating in a low-temperature oven. After the casting  
 281 and machining processes, the light guides were polished to a mirror surface  
 282 at the vendor with additional polishing performed at JLab only in the case of  
 283 scratches incurred during handling.

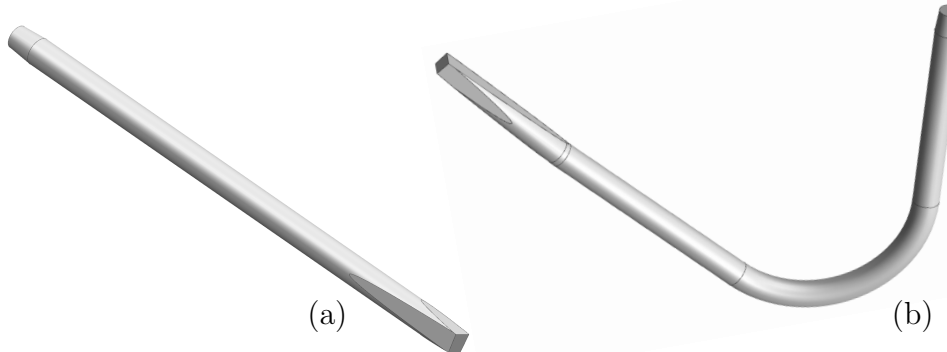


Fig. 8. The design of the CTOF (a) upstream and (b) downstream light guides. The wedge-shaped side of each figure is the end that couples to the scintillation bar and the cylindrical side of each figure couples to the PMT.

284 The design of the upstream light guide is shown in Fig. 8(a). The sides of the  
 285 Acrylic cylinder were milled to a length of  $\sim 25$  cm along the light guide to  
 286 form a wedge up to a radius of 37 cm in the  $(r, \phi)$ -plane in order to fit into the  
 287  $\Delta\phi = 7.5^\circ$  sector. The straight cylindrical section is  $\sim 75$  cm long to position  
 288 the PMT in the solenoid fringe field at a position where the maximum field is  
 289 at the level of  $\sim 1$  kG. The design of the downstream light guide is shown in  
 290 Fig. 8(b). The sides of the cylinder were milled to a length of  $\sim 30$  cm along  
 291 the light guide to form a wedge up to a radius of 40 cm in the  $(r, \phi)$  plane. The  
 292 light guide bends through an angle of  $135^\circ$  over a length of  $\sim 45$  cm around the  
 293 downstream face of the solenoid magnet to position the downstream PMTs in  
 294 a lower maximum value of the solenoid fringe field of about 400 G.

### 295 3.3.1 Monte Carlo Design Studies

296 The light guide design was optimized using a Monte Carlo program to simu-  
 297 late light propagation through the CTOF counter assemblies consisting of the  
 298 scintillation bar, the upstream and downstream light guides, and the PMT  
 299 entry windows. The transmittance of the light guide is a function of its mate-  
 300 rial properties, such as refractive index, bulk attenuation length, and surface  
 301 reflectivity. Additionally, the light guide transmittance depends on its geomet-

302 rical shape and size. In particular, the ratio of the light guide entrance area  $S_i$   
303 to its exit area  $S_o$  is of critical importance since Liouville's phase space the-  
304 oreom dictates that the transmittance  $T$  of the guiding system is constrained  
305 as:

306

$$T \leq \frac{S_o}{S_i}. \quad (1)$$

307 Thus, in order to avoid this fundamental limitation, the PMT photocathode  
308 area  $S_{pc}$  must be larger than the area of the end of the scintillation bar. For  
309 the CTOF system we required that  $S_{pc}$  be larger than  $\sim 12.5 \text{ cm}^2$ . For the  
310 R2083 PMT chosen for CTOF (see Section 3.4) with a 5.08-cm diameter and  
311 a  $16.6 \text{ cm}^2$  photocathode area, the cross section of the focusing light guide  
312 almost doubles from the scintillation bar end to the PMT. As was shown  
313 through both Monte Carlo calculations and light transmission measurements  
314 [12], this feature roughly doubles the transmittance of the focusing light guides  
315 compared to guides of a constant cross section.

316 The production light guides for CTOF were therefore based on a focusing de-  
317 sign where the cross section of the light guide matches to the wedge-shaped  
318 face of the scintillation bar and expands in cross section along its length to  
319 match the area of the PMT. The shape of such a light guide gradually trans-  
320 forms from a truncated pyramid with a trapezoidal cross section at the end  
321 of the scintillation bar to a cylinder in the middle part of the guide with area  
322  $S_c=20.3 \text{ cm}^2$ . It then maintains a constant cross section until very near the  
323 PMT location when it then becomes a truncated focusing cone that mates  
324 with the PMT as shown in Fig. 8.

325 We calculated the transport efficiency of the CTOF light guides using the  
326 BARTIM code (described in the Appendix of Ref. [13]) to track the photons  
327 through the system from their generation point in the scintillation bar until  
328 they crossed a material boundary or they interacted with a surface. At such  
329 an interface, the photon was then either totally internally reflected, reflected,  
330 or refracted according to the Fresnel equation. Imperfections on the surface of  
331 the scintillation bar or light guide were modeled by reducing the total inter-  
332 nal reflection coefficient,  $IR$ , below 100%. Any light that escaped from wall  
333 boundaries was specularly reflected with an appropriate reflection coefficient  
334  $R$ . Photons that were absorbed were tabulated as lost. At the boundary be-  
335 tween materials (e.g. scintillation bar - light guide, light guide - PMT), Snell's  
336 law was used to give the angle of the refracted photon. The process was re-  
337 peated over thousands of photons to gain sufficient statistics to make design  
338 choices.

339 The photons generated in the scintillation bar were modeled assuming minimum-  
340 ionizing particles normally incident on the middle of the CTOF counter. The

parameters used in our calculations were  $R=0.9$ ,  $IR=0.99$ , and a bulk attenuation length of  $\lambda_p=6.65$  m in the Acrylic. It was assumed that the wrapping was a radiant mirror film VM-2002 from 3M [14]. The simulation studies for the final production designs of the CTOF light guides yielded transmittances of  $\sim 60\%$  for the upstream light guides and  $\sim 50\%$  for the downstream light guides.

Each aspect of the light guide design was studied in detail to optimize its light transport efficiency. In the remainder of this section, some comments on different aspects of the design from the results of our Monte Carlo studies are highlighted.

- Light Guide Pitch Angles: The effect of changing the pitch angle of the upstream light guide from  $18^\circ$  to  $30^\circ$  was investigated. The transmission varied by less than 1%. Varying the downstream pitch angle was not investigated as a different pitch angle would violate the defined keep-out zones of the CTOF for both the solenoid and the high-threshold Cherenkov detectors.
- Light Guide Length: We investigated the effect of decreasing the light guide length by about 250 mm. The transport efficiency of the upstream and downstream light guides improved by  $\sim 10\%$  compared to our final design choice. However, the constraints on the CTOF from the neighboring detector subsystems and the practical design limits for the PMT magnetic shields, effectively set the positions of the PMTs and prevented a shorter light guide design from being employed.
- Extent of Wedge-Shaped Region: The transition of the light guides from the wedge-shaped end at the scintillation bar to the cylindrical cross section was optimized through Monte Carlo calculations. The design required that the light guides at the upstream and downstream ends of the detectors fully fit within a  $7.5^\circ$  opening from the target. The Monte Carlo calculations showed that the light transport efficiency is strongly dependent on the length of the cylindrical portion of the light guide. The longer the cylindrical portion of the light guide compared to the wedge-shaped region, the better the transmittance. For the upstream (downstream) light guides the wedge-shaped portion has an extent of  $\sim 25$  cm ( $\sim 30$  cm), which could not be made shorter and still have the light guide fit within its  $7.5^\circ$  azimuthal restriction.
- Light Guide to PMT Matching: The inner photocathode surface of the R2083 PMT used for the CTOF readout is part of a sphere with a radius of 2.3 cm. Due to this shape, the thickness of the entry window varies from 1 mm in the center to 7 mm at the periphery. Thus, the geometry of the PMT entry window needs to be taken into account since photons may escape through the periphery of the glass window, and according to our

Monte Carlo simulations, the PMT window effect may reduce the number of primary photoelectrons up to 30%. In order to compensate for this effect, the light guides transition from a constant cylindrical cross section to a focusing cone over their last  $\sim$ 5 cm. The focusing cone slightly increases the photon angle at the exit. Simultaneously, the cone shrinks the luminous area and provides for slightly better targeting at the photocathode. Since most of the photons at the end of the cylindrical part of the light guide propagate within the total internal reflection angle, the focusing cone directs a substantial fraction of the escaping photons to the spherical photocathode. The cone length and opening angle were optimized for the best possible transmittance.

### 3.3.2 Optical Tests of Acrylic

In order to evaluate the optical properties of the Acrylic light guides in terms of light transmittance, we developed a technique for rapid measurements using the setup shown in Fig. 9. We define the light transmittance of our light guides as the ratio of the light guide output radiation to input radiation. For our measurements we injected diffuse light of  $\sim$ 450 nm wavelength into the light guide along its axis from one end. At the opposite end we mounted an ILT1400 radiometer [15], which functioned as a photodetector. In order to determine the transmittance  $T$  we compared two measurements of the transmitted radiation  $R$ . The first value was measured with a very short reference light guide and the second value was measured with the light guide under study. This method automatically compensated for apparent light losses due to surface reflections. The transmittance of the light guide was computed as:

$$T = \frac{R(l_x)}{R(l_s)}, \quad (2)$$

where  $l_x$  is the length of the light guide (1 m upstream, 1.6 m downstream),  $l_s$  is the length of the short rod (2.5 cm), and  $R(l)$  is the transmitted light intensity measured with the sample of length  $l$ .

From these data for our upstream (downstream) light guides, we measured an average transmittance of  $\sim$ 60% ( $\sim$ 50%). Studies of our test setup indicated that our transmittance measurements were accurate to the few percent level. These values can be compared directly to measurements of the photoelectron statistics using cosmic ray data for a configuration with a CTOF scintillation bar coupled directly to a PMT to that where the scintillation bar is coupled to a production CTOF light guide. Our findings showed that the ratio of photoelectrons was  $\sim 60 \pm 5\%$  and  $\sim 50 \pm 5\%$  for the upstream and downstream light guides, respectively, in agreement with our bench measurements and our Monte Carlo calculation results discussed in Section 3.3.1.

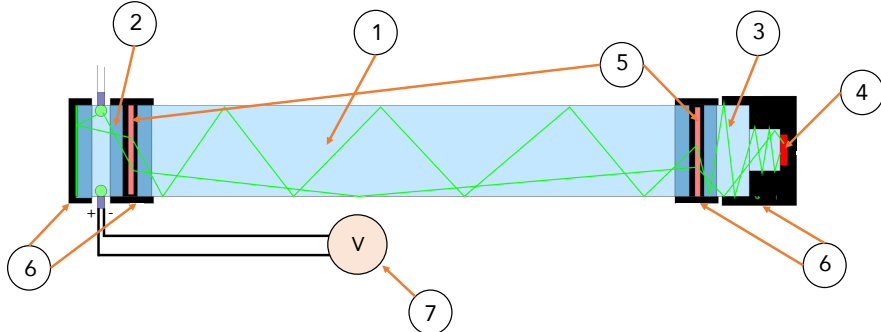


Fig. 9. (Color Online) CTOF setup for the light guide transmittance measurements. (1) Acrylic rod, (2) light source, (3) Acrylic piece, (4) silicon photodetector, (5) Teflon film as a diffuser, (6) mount units, and (7) digital voltmeter.

419 From the transmittance data the practical attenuation length (see Section 3.2  
 420 for a discussion of practical vs. bulk attenuation lengths) of the light guide  
 421 can be defined as:

$$422 \quad \lambda = \frac{(l_s - l_x)}{\ln(T)}, \quad (3)$$

423 which assumes an exponential attenuation of light along the light guide. The  
 424 average practical attenuation length measured for the CTOF Acrylic light  
 425 guides was  $\sim 2.3$  m.

426 In order to characterize the bulk attenuation length of our chosen Acrylic  
 427 material, the same measurement system shown in Fig. 9 was employed. For  
 428 these measurements the Teflon film light diffuser was removed. For this case  
 429 the sensor area of the photometer ( $\sim 1$  cm $^2$ ) was large enough to intercept  
 430 the full transmitted beam. The average bulk attenuation length of the Acrylic  
 431 material was measured to be  $6.65 \pm 0.5$  m.

### 432 3.4 Photomultiplier Tube/Voltage Divider Assemblies

433 The selection of the PMTs for the CTOF detector considered a number of dif-  
 434 ferent solutions, including both conventional PMTs and field-resistant PMTs.  
 435 Our final choice, which was thought to be the most conservative design, opted  
 436 for conventional PMTs contained within a magnetic shield system at the ends  
 437 of long light guides to position the PMTs well outside of the extremely high  
 438 field region of the solenoid magnet.

439 Our studies showed that the optimal light guide design should have an in-  
 440 creasing cross section from the scintillation bar to the PMT to optimize the  
 441 light transmission efficiency. Given the average surface area of the end face of  
 442 the scintillation bars of 11.45 cm $^2$ , we selected a 5.08-cm diameter PMT for

443 the readout. This corresponds to a surface area of 20.0 cm<sup>2</sup>. The size match-  
 444 ing comparison is shown in Fig. 10. Our choice for the CTOF readout was  
 445 the H2431 PMT/voltage divider assembly from Hamamatsu [16]. This inte-  
 446 grated assembly employs the 5.08-cm diameter Hamamatsu R2083 PMT [17].  
 447 The relevant specifications for this PMT are listed in Table 4. Fig. 11 shows  
 448 a schematic of the H2431 assembly and the circuit diagram for the voltage  
 449 divider.

450 For the R2083 PMT the diameter of the photocathode is 46 mm. As with  
 451 most timing PMTs, it has a spherical photocathode. Such a shape is helpful  
 452 to equalize path lengths of the primary photoelectrons to the first dynode.  
 453 However, due to this spherical shape, the accelerating electric field always has  
 454 a component perpendicular to an axial magnetic field. Therefore timing PMTs  
 455 like the R2083 are sensitive to the axial components of the magnetic fringe  
 456 field. The expectation for these PMTs is that they can operate in an envi-  
 457 ronment such that the maximum allowable axial field at the photocathode is  
 458 0.4 G. However, we have aimed to achieve fields of  $\leq 0.2$  G at the photocathode  
 459 to maintain a reasonable safety margin.

---

Spectral response	300 → 650 nm
Wavelength of max. emission	420 nm
Photocathode material	Bialkali
Minimum effective area	46 mm
Window material	Borosilicate glass
Dynode	8 stage, linear focused
Gain	$2.5 \times 10^6$
Quantum Efficiency @ $\lambda_{max}$	27%
Max. anode current rating	200 $\mu$ A
Anode dark current (typical)	100 nA
Anode pulse rise time	0.7 ns
Electron transit time	16 ns
Transition time spread	0.37 ns

---

Table 4

The properties of the Hamamatsu R2083 PMT used for the CTOF readout.

460 Alternative solutions for the PMTs were considered, specifically in terms of  
 461 field-immune and field-resistant devices. If such PMTs could be used (and  
 462 were competitive in terms of pricing compared to conventional PMTs), then  
 463 the CTOF could have been designed without the need for long light guides  
 464 or possibly without any light guides whatsoever. One solution considered em-  
 465 ployed the Burle 85011 micro-channel plate (MCP) PMT [19]. These devices

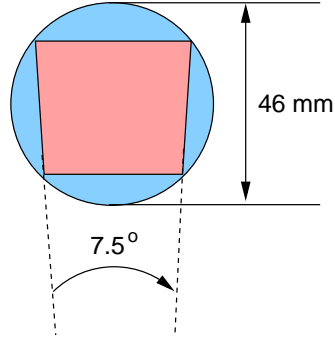


Fig. 10. (Color Online) The cross section of the end face of the scintillation bar (wedge cross section) inscribed into the photocathode of the R2083 PMT (circular cross section). The light guides match the shape of the scintillation bar on one end and the shape of the PMT on the other.

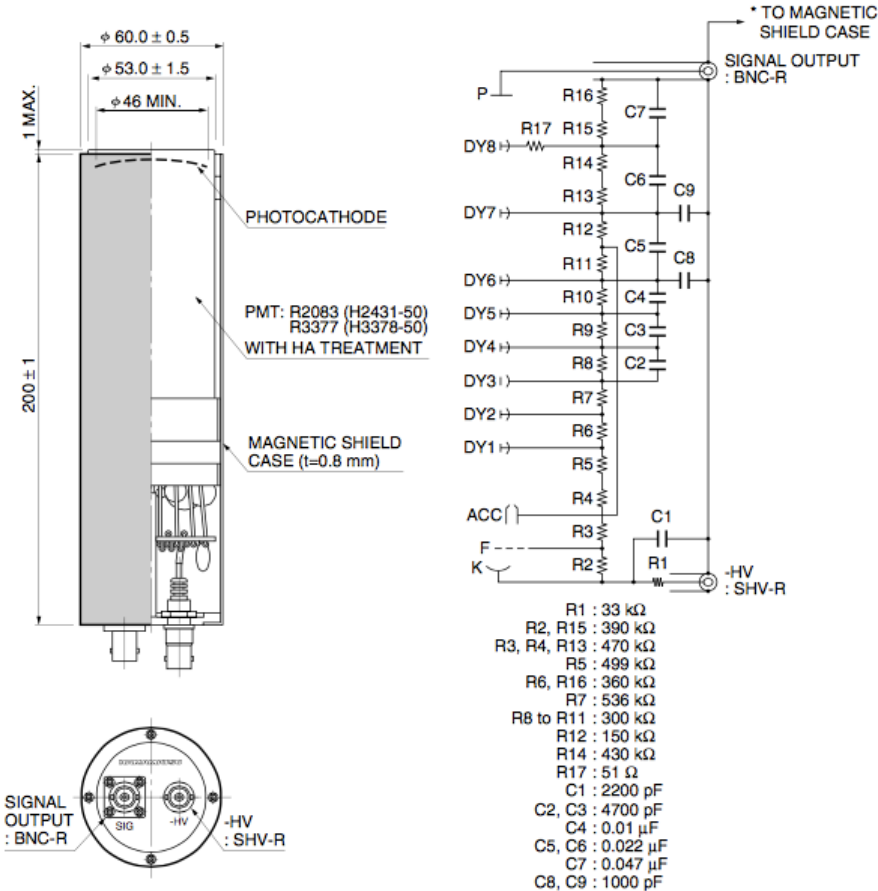


Fig. 11. Schematic diagram of the Hamamatsu H2431 assembly based on the R2083 5.08-cm diameter PMT used for the CTOF readout [18]. Note that for this application the supplied magnetic shield case was not used.

466 have immunity to magnetic fields up to  $\sim 2$  T, while providing very good timing  
467 resolution [20]. However, the drawback of MCP PMTs is that their quantum  
468 efficiency (QE) is only about half that of conventional PMTs, which would  
469 have an adverse affect on the counter timing resolution that has the behavior,

470

$$\sigma_{PMT} \propto \frac{1}{\sqrt{N_{ph} \cdot QE}}, \quad (4)$$

471 where  $N_{ph}$  is the number of incident photons at the photocathode of the PMT.  
472 From our studies the choice of a conventional PMT with a long light guide com-  
473 pared to an MCP PMT with no light guide gave comparable resolutions [21].

474 The issue of low QE of the MCP PMT can be solved with fine-mesh (FM)  
475 PMTs, which have been shown to operate in fields up to 1 T, or metal-channel  
476 (MC) PMTs, which hold promise of operating well in fields up to 0.2 T. With  
477 either the FM or MC PMTs as solutions for the CTOF, shorter light guides  
478 could be employed in the design.

479 Several different FM PMTs were studied during the CTOF design phase,  
480 including the R5505, R7761, and R5924 from Hamamatsu. These FM PMTs  
481 were shown to have stable timing response in external fields up to 1.2 T [22].  
482 The R5924 with photocathode size of 39 mm and the R7761 with photocathode  
483 size of 27 mm were poor matches to our required light guide dimensions. The  
484 R6504 with photocathode area of 51 mm, which has a dimension directly  
485 comparable to the R2083, however, was discontinued by Hamamatsu. In our  
486 studies that directly compared the intrinsic time resolution of the R2083 to the  
487 R5924 using an LED source with each PMT seeing exactly the same amount  
488 of light, the resolution of the R5924 was found to be roughly a factor of two  
489 worse than the R2083. These findings were confirmed in beam studies in Hall B  
490 at JLab [23].

491 We also considered MC PMTs such as the H8500 and R7400 from Hamamatsu.  
492 These devices have excellent timing characteristics (with a transition time  
493 spread  $\sigma_{TTS}=400$  ps), comparable QE to conventional PMTs, and have been  
494 shown to be able to operate in external fields up to 0.2 T. The technical issue  
495 with the MC PMT is that its intrinsic gain is roughly a factor of three smaller  
496 than for the R2083 and signal to noise ratio concerns become an issue.

497 *3.4.1 Rate-Stabilized Divider*

498 The voltage divider circuit shown in Fig. 11 is a standard inclusion with the  
499 R2083 PMT in the Hamamatsu H2431 assembly. Due to the requirement of  
500 stable PMT performance in terms of gain and timing response in the high rate  
501 environment of the CTOF detector just outside of the beam-target interaction

502 region, we have made a small modification to the stock Hamamatsu divider  
 503 to improve its stability to higher currents. A small amplifier circuit has been  
 504 inserted as a sequential component after the last resistor in the divider. This  
 505 active division circuit consists of two transistors that are powered by the cur-  
 506 rent flowing through the divider. A version of this circuit design is described  
 507 in Ref. [24].

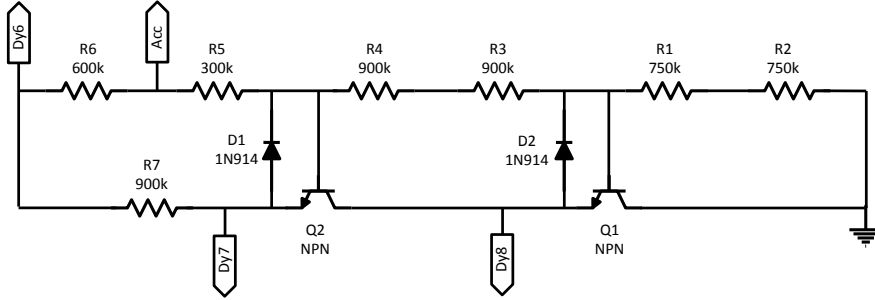


Fig. 12. Schematic diagram of the JLab-designed transistorized impedance matching amplifier circuit added to the standard Hamamatsu R2083 voltage divider.

508 The active divider circuit is an amplifier that is actually an impedance con-  
 509 verter, which provides an output impedance termination matching to a stan-  
 510 dard  $50\ \Omega$  coaxial cable. The active divider circuit is mounted on a small  
 511 mezzanine board that is soldered into the stock R2083 divider. It is connected  
 512 to Dy6, Dy7, Dy8, ACC (see Fig. 11), and grounded as shown in the circuit  
 513 schematic of Fig. 12. The passive divider resistors connected to those dynodes  
 514 were removed and all capacitors were left in place. The transistors employed  
 515 are high voltage (400 V or better rated) Si NPN types.

516 Fig. 13 compares the performance of the stock R2083 voltage divider from  
 517 Hamamatsu to that of a typical modified divider. This figure shows a compari-  
 518 son of the gain stability of the PMT/divider assemblies as a function of the  
 519 PMT anode current. The gain of the modified divider is seen to be more in-  
 520 dependent of current up to  $200\ \mu\text{A}$ , the maximum rated current of the device,  
 521 compared to the stock divider. Fig. 13 also shows a corresponding improve-  
 522 ment in the stability of the timing response up to  $200\ \mu\text{A}$ .

### 523 3.5 Magnetic Shields

#### 524 3.5.1 CLAS12 Solenoid Field

525 The CLAS12 solenoid is a self-shielded superconducting magnet that is used  
 526 to produce a field primarily along the beam direction about the target. The  
 527 magnet has an inner diameter of 100 cm and is roughly 1.5 m long. The central

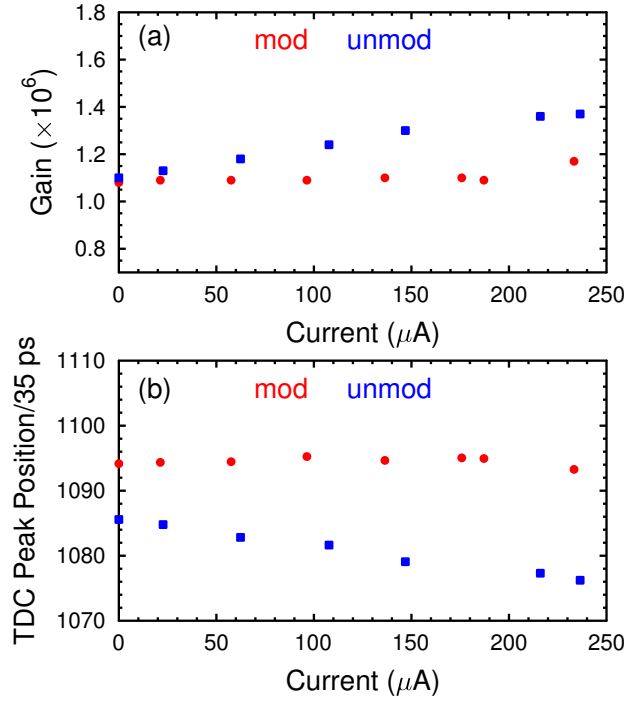


Fig. 13. (Color Online) Comparison of the performance of the R2083 PMT vs. PMT anode current ( $\mu$ A) with its stock divider (blue squares) compared to that of an R2083 PMT with the modified divider (red circles) showing (a) the gain stability and (b) the timing response stability.

528 field of the magnet is 5 T at its nominal full current. Outside the magnet a  
 529 sizable fringe field extends for several meters in all directions. Given the many  
 530 design constraints for the CLAS12 Central Detector region that essentially  
 531 localized the positions of the CTOF counter elements, the PMTs are located  
 532 in fringe fields from the solenoid at levels up to  $\sim$ 1 kG.

533 To determine the necessary shield reduction factors at the locations of the  
 534 PMTs, the field values at the locations of one upstream high-pitch angle and  
 535 one low-pitch angle PMT were determined using a map of the CLAS12 solenoid  
 536 fringe field was based on a full 3-D finite-element analysis calculation using  
 537 the OPERA-TOSCA suite [25] to model the magnet. Note that due to the  
 538 azimuthal symmetry of the solenoid fringe field, the field strengths and gradi-  
 539 ents at the locations of the full set of CTOF upstream PMTs can be assumed  
 540 to be the same. Table 5 provides the field components of the CLAS12 solenoid  
 541 fringe field at the locations along the axis of the PMT at the photocathode  
 542 (i.e. the face of the PMT), the first dynode (a distance 3 cm from the pho-  
 543 tocatheode), and the middle of the accelerating structure (a distance 5.5 cm  
 544 from the photocathode) for both PMTs. All of the fields are necessarily given  
 545 without any shields present as the shields strongly modify the local fringe field  
 546 distributions. Table 5 also includes the field components along the PMT axes  
 547 at the locations of the end faces of the shield assemblies. Shield end #1 is

548 the end closest to the magnet and shield end #2 is the end farthest from the  
 549 magnet. For shield end #1, the strength of the field for the high-pitch angle  
 550 design is 1000 G and for the low-pitch angle design is 1076 G. However, due  
 551 to the different positions of these shields in the solenoid fringe field, the corre-  
 552 sponding axial and transverse field components at these locations for the two  
 553 designs are significantly different.

	High-Pitch Angle	Low-Pitch Angle
Position	$(B_y, B_z)$	$(B_y, B_z)$
Shield End #1	(981, 192) G	(956, 493) G
Photocathode	(612, 118) G	(632, 329) G
First Dynode	(491, 93) G	(490, 27) G
Middle Dynode	(405, 85) G	(416, 221) G
Shield End #2	(337, 78) G	(342, 193) G

Table 5

Magnetic field components along the central axis of a representative upstream CTOF PMT of the high-pitch angle and the low-pitch angle designs positioned in the  $(y, z)$  plane in the CLAS12 coordinate system ( $y$ -axis points up,  $z$ -axis is along the beamline). The associated field components are from a 3-D field map of the CLAS12 solenoid. The positions are locations along the associated PMT axes at the photocathode, the first dynode, the middle of the accelerating structure, and at the end faces of the magnetic shield volumes.

554 For the positioning of the CTOF magnetic shields in the CLAS12 solenoid  
 555 fringe field, the field lines are at roughly  $40^\circ$  with respect to the axis of the  
 556 PMT. In this case roughly two-thirds of the field is axial, which produces a  
 557 smaller effect on PMT performance than the transverse component, but is  
 558 more difficult to shield.

559 We do not consider here the PMTs at the downstream end of the magnet.  
 560 However, using the field map and the known downstream PMT locations, the  
 561 maximum field strength for the downstream PMTs within the shield volume  
 562 is  $\sim 400$  G. Because we have opted to use an identical shield for all CTOF  
 563 PMTs, the discussion here focuses only on the shield design for the upstream  
 564 PMTs. A shield designed for the fields seen at the upstream PMT locations  
 565 will necessarily work to shield the lower field seen at the downstream PMT  
 566 locations.

### 567 3.5.2 Shield Design

568 The timing performance of PMTs in external magnetic fields deteriorates due  
 569 to the Lorentz force. After an external photon hits the surface of the pho-  
 570 tocatheode and knocks out a primary photoelectron, the electron accelerates

571 toward the first dynode along the electric field lines. In most timing PMTs, the  
572 photocathode is shaped as a segment of a sphere. The first dynode is located  
573 close to the center of this sphere where the electric field lines concentrate.  
574 This design provides for equal travel times for the electrons created at differ-  
575 ent parts of the photocathode. However, even an axial magnetic field has a  
576 transverse component to the electric field, and Lorentz forces affect both the  
577 propagation time and the destination of the electrons, depending on the de-  
578 sign of the accelerating electrode. In designing magnetic shields for the CTOF  
579 PMTs, we have been careful to consider both axial and transverse magnetic  
580 field components.

581 Various multi-layer shield designs for the CTOF PMTs were studied that were  
582 comprised of different coaxial ferromagnetic cylinders. Ultimately we found  
583 that a 28-cm-long, three-layer shield composed of 1008 steel of maximum thick-  
584 ness of 1.7 cm for the outer layer, a 3-mm-thick layer of the ferromagnetic  
585 HiPerm-49 for the middle layer, and a 0.8-mm-thick layer of the ferromag-  
586 netic Co-NETIC for the inner layer, provided the best performance within the  
587 CTOF magnetic field environment. Modeling calculations and measurements  
588 with physical prototypes showed that such a shield design can reduce a 1 kG  
589 external axial field to the level of  $\sim$ 0.5 G at the location of the PMT. To reduce  
590 the remaining remnant field to the level of  $\sim$ 0.2 G, a compensation solenoid  
591 coil is included just outside of the inner ferromagnetic layer. The design of the  
592 magnetic shield system for the CTOF PMTs is discussed in Refs. [26,27].

593 In order to make the magnetization more uniform across the outer shielding  
594 cylinder, an improved design has been realized by using a tapered cylinder  
595 1.0 cm thick at the ends and 1.7 cm thick in the middle. Since both the mag-  
596 netic field flux and the material thickness increase linearly toward the middle  
597 of the cylinder, the magnetic field density in the shield layer is almost constant.  
598 This maximizes the permeability and results in significantly lower and more  
599 uniform fields inside the cylinder, which improves the shielding capability of  
600 the inner layers.

601 Ferromagnetic materials for shielding applications are of two types, those with  
602 high saturation and those with high permeability. In very high fields, materials  
603 with high saturation should be used. This is the reason why we chose 1008  
604 steel for our outermost shield layer. In moderate fields, ferromagnetics with  
605 high permeability can be used. The alloy HiPerm-49 (48% Ni, 0.5% Mg, 0.35%  
606 Si, 0.02% C, balance Fe) was chosen, which has a saturation flux density of  
607  $\sim$ 1.5 T after hydrogen annealing. Thin cylinders made of high permeability  
608 materials are useful in small magnetic fields. For the inner shield layer Co-  
609 NETIC was selected, an alloy that contains 80.6% Ni and 14% Fe, which  
610 saturates at about 0.8 T and is in the same family metallurgically as  $\mu$ -metal.

611 Using coaxial cylinders meets the design requirement that the magnetic shields

612 have openings for the coaxial light guides. Therefore, axial field lines can easily  
613 penetrate inside the shield. In order to eliminate this effect, an approach has  
614 been developed using a combination of passive and active elements. In this  
615 design, the compensating solenoid that makes up the active element controls  
616 the magnetization of the ferromagnetic layers, including the innermost shield  
617 layer, which determines the field within the PMT (see Section 3.5.3).

618 Fig. 14 shows a cut-away view of the CTOF PMT shield system from our  
619 3-D design model to highlight the components that make up the different  
620 layers and their positioning with respect to each other. The inner shield layers  
621 are attached to the light guide using a supporting clamp and the steel shield  
622 layer is attached to a support structure secured to the CLAS12 solenoid. Note  
623 that both the external and the intermediate shield layers actually consist of a  
624 cylindrical section with conical endcaps that fit tightly together. The conical  
625 endcaps help to capture more field lines at low radial coordinates compared to  
626 a flat cylinder. This feature results in a lower inner field with better uniformity  
627 along the central axis. The PMT itself fits within the inner shield cylinder and  
628 the light guide feeds into the opening on the downstream end of the shield  
629 assembly. The full weight of each shield assembly is  $\sim$ 40 lbs.

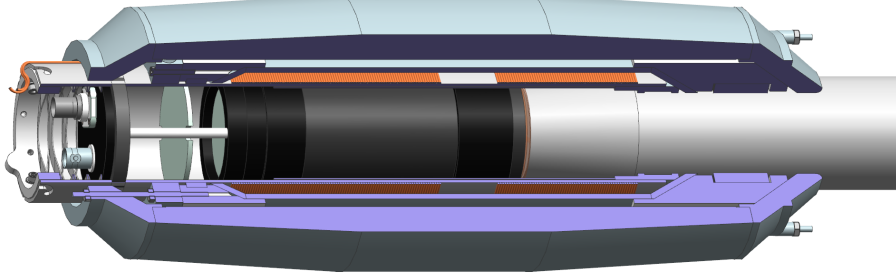


Fig. 14. (Color Online) The CTOF shield as shown in a 3-D cut-away view. The black cylinder in the middle of the shield is the PMT. The light guide enters the shield from the right-hand side. The two orange bands outside the PMT are the compensation coils.

### 630 3.5.3 Compensation Coils

631 A compensation coil of 150 turns of 1-mm-thick magnet wire (18 AWG cop-  
632 per with a polyurethane and polyimide overcoat) was wound on an aluminum  
633 mandrel that was positioned between the inner and middle ferromagnetic lay-  
634 ers. The compensation coil actually consists of two wholly independent coils,  
635 the first  $z_1$  of 90 turns placed about the middle of the PMT accelerating struc-  
636 ture and the second  $z_2$  of 60 turns placed about the PMT photocathode. A  
637 gap between the coils was included to achieve a more uniform field along the  
638 PMT axis. 2-D FEA calculations showed that coil currents on the order of  
639 0.5 A to 1 A were sufficient to reduce the inner remnant field of 0.5 G to 1 G

640 down to the level of 0.2 G for optimal PMT response. For these currents, the  
 641 coils generate a field of 5 G to 10 G at the surface of the mandrel.

642 It should be emphasized that the compensation coils are placed outside of  
 643 the innermost ferromagnetic cylinder. The whole point is that the effective  
 644 field in the PMT area is a superposition of the ferromagnetic magnetization,  
 645 the residual external fields, and the coil field. Unlike the case of an external  
 646 compensation coil, the inner coil positioning creates two opposite axial fields.  
 647 The first field is the field of the compensation coil and the second field with  
 648 the opposite direction is due to the additional ferromagnetic magnetizations  
 649 by the compensation coil. Field calculations were carried out to show that the  
 650 two opposing fields reduced the field along the PMT accelerating structure  
 651 from  $\sim 1$  G down to  $\sim 0.2$  G.

652 For the CTOF shields the compensation coils  $z_1$  and  $z_2$  are independently  
 653 controllable. The low voltage power supply for the coils is a Wiener MPOD  
 654 mini-crate outfitted with two MPV8016I modules [28]. Each module has eight  
 655 channels that can individually provide up to 50 W per channel with a max-  
 656 imum current of 5 A. The power supply is connected to the coils through  
 657 15 – 21 m long power cables. Fig. 15 shows the power circuit layout. The  
 658 system has been tuned for six different values of currents in  $z_1$  and  $z_2$  cor-  
 659 responding to the upstream low-pitch angle shields, the upstream high-pitch  
 660 angle shields, and the downstream shields.

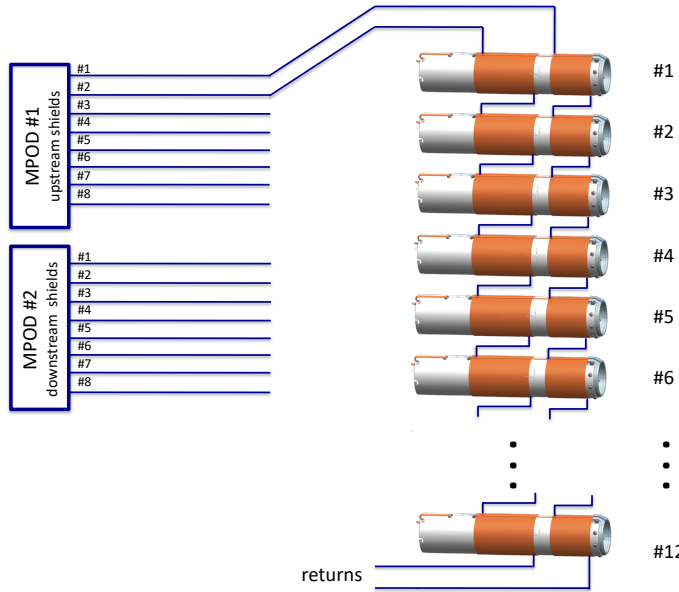


Fig. 15. (Color Online) Layout of the power circuit for the CTOF magnetic shield compensation coils.

661 Although the Wiener MPOD system can provide up to 5 A per channel, our  
 662 field test studies (see Section 3.5.5) showed that typical coil currents of the

663 level of 0.5 A to 1 A were appropriate for shield operation. In this current  
664 regime the coil system remains at room temperature. During operation of  
665 the coil power supply in Hall B, a temperature interlock circuit protects the  
666 coils from overheating by shutting off the MPOD power supply if the shield  
667 temperature at the mandrel location goes about 100 °F.

668 *3.5.4 Model Calculations*

669 In order to optimize the performance of the CTOF magnetic shields, studies  
670 were performed using both 2-D and 3-D finite element analysis (FEA) calcula-  
671 tions. Ultimately, full consistency between these approaches was achieved [27].  
672 The 2-D FEA calculations were carried out using the Poisson Superfish pro-  
673 gram [29]. In this model the shield was placed into an axial field with a gradient  
674 along the shield axis to approximate a realistic CLAS12 field scenario. For this  
675 calculation the maximal external field was  $\sim$ 1300 G at the side of the shield  
676 nearest the solenoid and  $\sim$ 700 G at the opposite end. The magnetic field in  
677 the accelerating area of the PMT was below 1 G without the compensation  
678 coils energized.

679 Full 3-D calculations with the OPERA-TOSCA suite [25] for the CTOF shields  
680 in a 1 kG uniform external field titled at 40° with respect to the shield axis  
681 yielded the results shown in Figs. 16 and 17. Fig. 16 plots the field profile as a  
682 function of transverse coordinate across the shield system at the location of the  
683 photocathode, the first dynode, and the middle of the accelerating structure.  
684 Fig. 17 plots the field profile as a function of axial coordinate along the shield  
685 system. The different curves correspond to coordinates near the inner cylinder  
686 walls and along the PMT symmetry axis.

687 Fig. 16 shows that as the outer shield layer is approached moving toward the  
688 PMT, the field magnitude slightly changes and that the behavior depends  
689 on the coordinate along the axis. Inside the outer ferromagnetic layer, the  
690 field magnitude rises up by a factor of 10 to  $> 10^4$  G due to the very high  
691 magnetization of the ferromagnetic material that may be close to saturation.  
692 In the region between the outer and middle ferromagnetic cylinders, the field  
693 magnitude drops by a factor of 10-50 depending on the axial coordinate along  
694 the shield. A similar effect is seen between the middle and the inner layers.  
695 At the location of the PMT the field magnitude is  $\sim$ 0.4 G. Note that the  
696 compensation coils were not energized for these calculations.

697 Fig. 17 shows an essentially monotonic decrease of the field strength moving  
698 along the axial coordinate that contains the shield toward the region where the  
699 PMT is located. The calculations show that the remnant field at any position  
700 within the PMT accelerating area ( $\pm$ 4 cm about 0) is below 0.5 G. Again this  
701 calculation was performed with the compensation coils turned off.

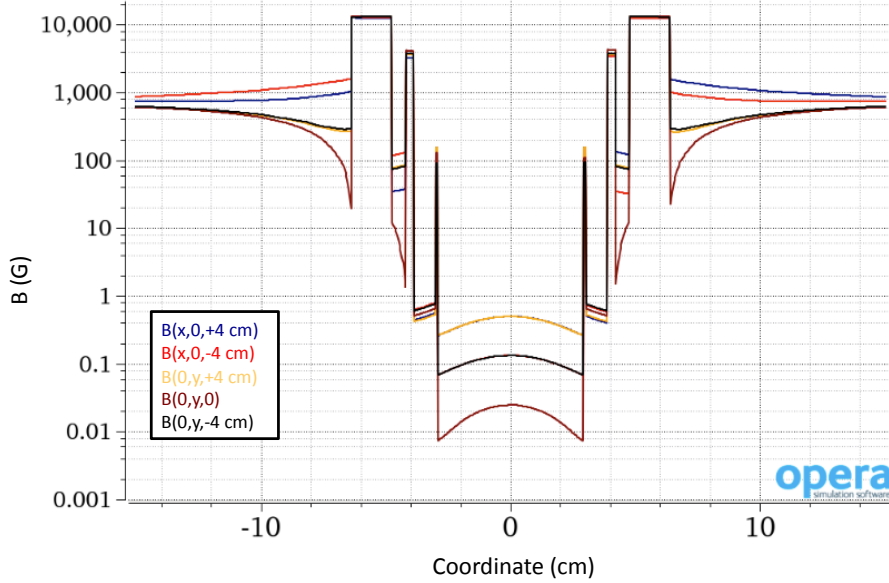


Fig. 16. (Color Online) 3-D magnetic field calculations using the code suite Opera [25] for the CTOF PMT shield in a uniform 1 kG field. The calculation plots the field profile (in G) across the transverse coordinate (in cm) of the CTOF three-layer passive magnetic shield system. The different curves correspond to different transverse coordinates along the PMT (photocathode at  $z=+4$  cm, first dynode at  $z=0$ , and middle of the accelerating structure at  $z=-4$  cm). For this calculation the external field lines were at an angle of  $40^\circ$  relative to the shield axis of symmetry to reflect the expected operational configuration of the shields.

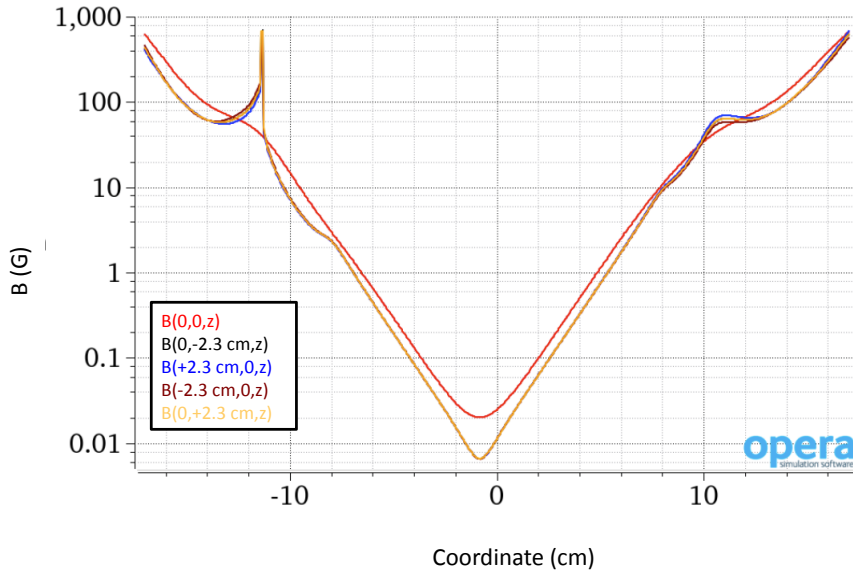


Fig. 17. (Color Online) 3-D magnetic field calculations using the code suite Opera [25] for the CTOF PMT shield in a uniform 1 kG field. The calculation plots the field profile (in G) at coordinates across different axial lines at  $y = \pm 2.3$  cm. For this calculation the external field lines were at an angle of  $40^\circ$  relative to the shield axis of symmetry to reflect the expected operational configuration of the shields.

702    3.5.5 *Shield Testing*

703    In order to validate the 2-D and 3-D FEA calculation results for the CTOF  
704    magnetic shield design, studies were completed placing one of the shields in  
705    the fringe field of a 5-T superconducting test magnet (30 cm long, 12.7 in  
706    diameter bore). For these tests the goal was to place the CTOF shield in  
707    the fringe field at positions that matched the field strength and gradient for  
708    what was expected from Table 5 for the shield positioning in the fringe field  
709    of the CLAS12 solenoid. Tests were performed in field conditions that well  
710    matched those expected for the high-pitch angle and low-pitch angle upstream  
711    PMTs. The full results from these tests are detailed in Ref. [30]. Note that  
712    the downstream CTOF PMTs are positioned in a region of the solenoid fringe  
713    field that is more than a factor of two lower than for the upstream PMTs. For  
714    this reason this configuration was not studied.

715    The first set of measurements was carried out with the compensation coils  
716    turned off to evaluate the passive shield layers. The data collected clearly  
717    show the efficacy of the shield system design. The tests showed that all field  
718    components were measured to be less than 0.5 G at all positions along the  
719    PMT volume. Studies of the effect of the compensation coils on affecting the  
720    internal field along the PMT location were completed with coil current settings  
721    of up to 1 A (with  $i_{z_1} = i_{z_2}$ ). The studies showed that the compensation coils  
722    could be adjusted to reduce the internal remnant fields to levels of  $\sim 0.2$  G  
723    even in the studies with up to nearly two times higher external fields.

724    3.6 *Assembly*

725    The CTOF counter assembly employed a precision alignment table config-  
726    urable to match the geometry of the CTOF counters with both the high-pitch  
727    angle and the low-pitch angle upstream light guides. This assembly table was  
728    designed to position the counter light guides and scintillation bar into their  
729    proper alignment for gluing. To bond the pieces together Bicron BC-600 opti-  
730    cal cement [31] was employed. Each counter was left to cure for 24 hours after  
731    application of the epoxy. Note that our bench tests showed that the scintil-  
732    lator/light guide joints made up with BC-600 were 30% stronger than using  
733    Dymax 3-20262 UV curing glue [32].

734    After gluing of the counters was completed, they were placed onto storage  
735    carts in the CTOF assembly area. These carts each held eight counters laid  
736    horizontally in a vertical stack with  $\sim 20$  cm between each counter. The next  
737    step in the counter preparation was to wrap the counters, first in a highly  
738    reflective layer and then in a fully opaque layer. The highly reflective wrap-  
739    ping layer for the CTOF counters employs the Enhanced Specular Reflector

740 VM-2002 [33]. This layer serves to increase the light transmittance along the  
741 counter from the charged particle ionization path to the PMTs. The outer  
742 opaque layer for the CTOF counters employs Tedlar, a polyvinyl fluoride film  
743 from DuPont [34].

744 The nominal gap between the bare faces of neighboring CTOF scintillation  
745 bars in the barrel is 800  $\mu\text{m}$ . In order to have sufficient space to form the  
746 barrel at its nominal radial position allowing for assembly and component  
747 tolerances, it was imperative that the wrapping be completed so that there  
748 were no wrinkles or excess material on the inter-counter sides of the bars and  
749 that all tape seals were applied only to the inner and outer radial surfaces  
750 of the bars. To aid in this required the VM-2002 sheets to be pre-formed  
751 using templates that made precise creases that matched the wedge-shape of  
752 the scintillation bars of the two different designs (low-pitch angle bar and  
753 high-pitch angle bar - see Section 3.1).

754 The scheme for wrapping the Tedlar layer on the scintillation bars was based  
755 on cold-forming Tedlar templates using tooling designed to give precise Tedlar  
756 forms that could be mated to the counters and sealed with electrical tape  
757 along smooth, wrinkle-free seams. This region covers the scintillation bar and  
758  $\sim 30.5$  cm of the transitions from the tapered to the cylindrical portions of  
759 the upstream and downstream light guides. The remaining portions of the  
760 Tedlar wrapping that span from the template region of the counters to the  
761 PMTs was easily covered using rectangular pieces of Tedlar wrapped around  
762 the cylindrical light guides. The full details on the counter wrapping for the  
763 scintillation bars is included in Ref. [35]. The final inter-counter gap after  
764 wrapping is  $\sim 450$   $\mu\text{m}$  on average ( $= 800 \mu\text{m} - 2 \times 50.8 \mu\text{m}$  (Tedlar outer-wrap)  
765 -  $4 \times 66.0 \mu\text{m}$  (VM-2002 inner-wrap including overlap of sheets)).

766 After the counter wrapping was completed, the counters were secured in their  
767 positions on the storage carts and the magnetic shields were installed. Due to  
768 the weight of the shield assemblies, they were designed to be assembled for  
769 counter testing without the heavy steel cylinder and its associated upstream  
770 steel cone (see Fig. 14). These pieces were not attached to the counters until  
771 they were moved to Hall B for installation into the solenoid using the CTOF  
772 installation strongback that supported the weight of the shields. The instal-  
773 lation procedure for the counters is detailed in Section 3.7. Full details on  
774 the procedures for assembly of the CTOF magnetic shields are included in  
775 Ref. [36].

776 With the inner and intermediate shield layers installed on each light guide, the  
777 final step of the counter assembly was to install the R2083 PMTs with their  
778 voltage dividers into the shield volume. Note that the azimuthal orientation  
779 of the PMT within the Co-NETIC shield layer takes is set to minimize  $\vec{v} \times \vec{B}$   
780 effects from the remnant solenoid field within the shield volume that might

otherwise result in loss of photoelectrons from the acceleration chain. The coupling contact between the PMT and the end of the light guide was made up with BC-630 silicone optical grease [37] ( $n=1.465$ ) to match the indices of refraction of the two materials. The PMT was held against the light guide using pressure from a spring clamp at the end of the voltage divider (see Fig. 14).

The storage carts served as the basis for the CTOF cosmic ray test stand and extensive characterization of the counters and their performance were completed during the year between the completion of counter assembly and installation in Hall B. The results of the cosmic ray studies in the assembly area are detailed in Section 4.

### 3.7 Installation

Due to the geometry of the CTOF counters, they were inserted into the solenoid magnet one at a time, with the insertion taking place from the downstream end of the solenoid. The counter installation consisted of four steps as detailed below and illustrated in Fig. 18.

Step #1: The counter was placed on the heavy shield attachment table and the outer steel shield cylinders were installed. The installation strongback was attached to the counter. The full shield assemblies were fully supported by the strongback with no stress on the counter itself. The counter was then craned from the floor of Hall B and the strongback was attached to the installation arm of the CTOF installation cart that moved along a set of rails used for moving the solenoid magnet. Initially the cart was moved well downstream of the solenoid (which had been moved  $\sim 10$  m upstream of its nominal operating position). The counter and strongback were supported on the installation arm pivoted to the counter installation position as shown in Fig. 18(a).

Step #2: The cart was moved upstream to insert the counter into the solenoid volume. The installation arm was then rotated to the desired azimuthal location after the cart hit the rail stop positioned along the solenoid rails at the proper installation position as shown in Fig. 18(b).

Step #3: The counter installation arm was then pivoted until the CTOF scintillation bar was horizontal and the pieces that mate with the support structure matched up and engaged as shown in Fig. 18(c).

Step #4: The load of the shields was transferred from the strongback to the CTOF support structure. The attachment bolts were engaged through slots in the support structure that allowed for the counter to be adjusted to its final position. The strongback was then freed and the installation arm was pivoted

818 back to its insertion position, allowing the cart to be pushed back downstream  
819 and reset for the next counter as shown in Fig. 18(d).

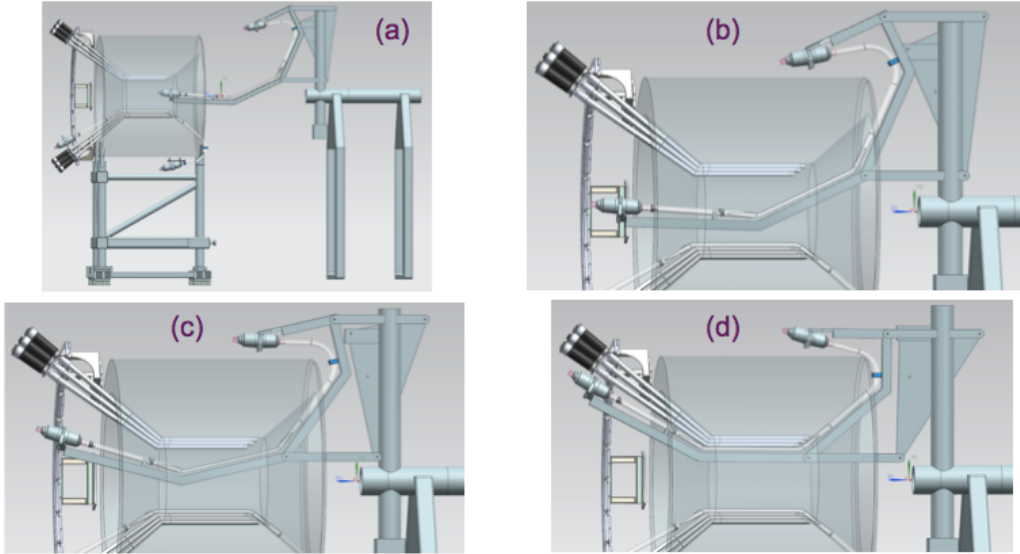


Fig. 18. [Replace] (Color Online) Steps in the CTOF counter installation sequence.  
(a) Mount counter to installation cart, (b) Move counter into solenoid from the downstream end and rotate in azimuth to proper position, (c) Pivot counter radially into proper installation position, (d) Attach the counter to the support structure.

820 The installation sequence proceeded with installing the counters in quadrants,  
821 starting at the bottom position on the solenoid and installing counters alter-  
822 nating back and forth between the high-pitch angle and low-pitch angle de-  
823 signs. The final counter for insertion (with the low-pitch angle design) was  
824 machined to have a rectangular cross section of 24 cm width to fit into the  
825 last gap in the barrel.

826 After installation of each counter, survey measurements were taken to en-  
827 sure counter positioning was within tolerances and any adjustments necessary  
828 were made. The final survey of the counters after installation and adjustments  
829 showed that all counters were positioned radially to within  $\pm 3$  mm of their  
830 design position. The final counter-by-counter radial offsets were included in  
831 the CTOF geometry tables used for event reconstruction. The signal and high  
832 voltage cables were attached after all counters were installed. This was followed  
833 by attachment of the power connections to the magnetic shield compensation  
834 coils.

835 *3.8 Electronics*

836 The CTOF counters generate prompt signals for pulse-height and timing anal-  
837 ysis. The anode from each PMT is connected to a passive signal splitter. 20%

838 of the anode pulse is fed to a JLab-designed analog-to-digital converter flash  
 839 ADC (FADC). 80% of the anode pulse is fed to a constant fraction discrimi-  
 840 nator connected to a high-resolution time-to-distance converter (TDC). The  
 841 overall layout of the CTOF electronics that processes these signals is shown  
 842 in Fig. 19.

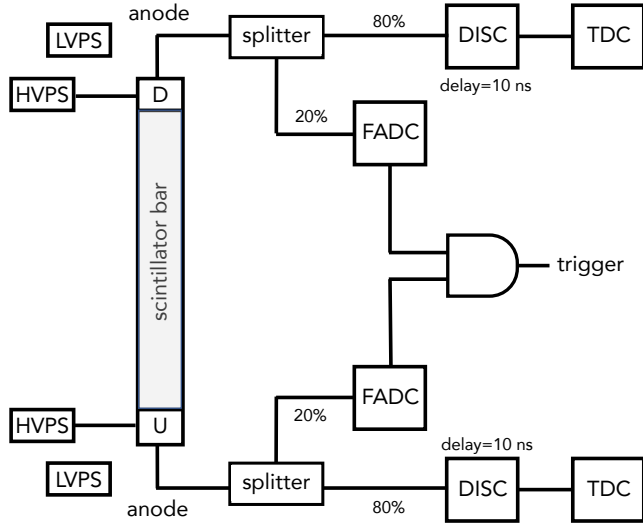


Fig. 19. Block diagram showing the layout of the readout electronics and power connections for a single CTOF counter.

843 Due to the limited number of channels in the CTOF system, the decision  
 844 was made to employ constant fraction discriminators (CFDs) for the readout.  
 845 The constant fraction technique permits optimal timing measurements to be  
 846 made without the need for sizable offline time-walk corrections to remove the  
 847 effects of time offsets due to pulses of different amplitudes crossing threshold  
 848 at different times.

849 For the CTOF system Ortec 935 4-channel 100 MHz CFDs [38] are employed.  
 850 The single-width NIM modules accept negative input pulses and generate three  
 851 simultaneous NIM-standard fast negative logic pulses for each input pulse that  
 852 exceeds the set threshold level. The unused bridged outputs are terminated  
 853 into  $50 \Omega$  as recommended by the manufacturer.

854 The constant-fraction shaping delay for each discriminator channel is deter-  
 855 mined by the length of external  $50 \Omega$  coaxial cable connected to the channel  
 856 shaping circuit. To select the optimal shaping delay the counter timing res-  
 857 olutions were studied for delay cables from 4 ns to 16 ns for each counter  
 858 relative to a fixed reference time. Fig. 20 shows the results of these studies  
 859 for a set of 8 counters. The resolution was seen to improve until a minimum  
 860 is reached and then remains relatively flat. The final delay setting employed  
 861 10 ns delay cables (with the internal module offset delay omitted) with the

862 time-walk compensation network setup according to the manufacturer's rec-  
 863 ommendations.

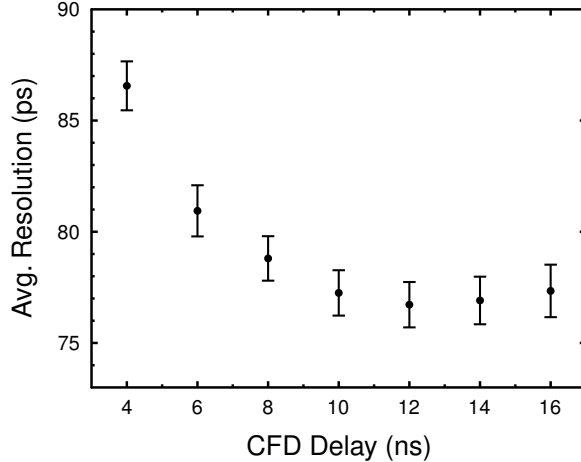


Fig. 20. Average resolution for a set of 8 CTOF counters (ps) vs. CFD shaping delay (ns).

864 During operation of the CTOF system in Hall B, the CTOF discriminator  
 865 thresholds were set to  $\sim 30$  mV. After setting the PMT gains, this corresponded  
 866 to a threshold of  $\sim 1$  MeV of deposited energy. This threshold is well below the  
 867 6 MeV energy deposited by a normally incident minimum-ionizing particle.

868 The output of the discriminator goes to a CAEN VX1290N 16-channel 25 ps  
 869 LSB (least significant bit) VME TDC [39]. These multi-hit pipeline TDCs were  
 870 chosen in order to allow for readout capability in the operating luminosity of  
 871  $1 \times 10^{35} \text{ cm}^{-2}\text{s}^{-1}$ . The TDC readout window was set to 250 ns to ensure the  
 872 full dynamic range of the data was safely in time with the trigger. The key  
 873 performance specifications of these units are given in Table 6.

874 The integral non-linearity (INL) of the TDCs represents the accumulated er-  
 875 ror of the input-output characteristic of the TDC with respect to the ideal  
 876 response. This is defined by the function:

$$877 D(t) = \int \frac{t}{LSB}, \quad (5)$$

878 where  $D$  is the output data,  $t$  is the input time, and  $LSB$  is the bin size. The  
 879 compensation tables for the CAEN V1190A and VX1290A TDCs are stored as  
 880 tables in the unit SRAM memory. Initial tables are measured at the factory  
 881 and come preloaded on the modules. These tables are reasonably accurate  
 882 when reading out the module using its internal 40 MHz/25 ns period clock.  
 883 However, in CLAS12, the modules are strobed with a clock of a slightly larger  
 884 frequency of 41.67 MHz. This difference in the frequency has a non-negligible  
 885 affect the INL tables. For our purposes we use a high frequency pulser to  
 886 populate the full dynamic range of the TDC within the CLAS12 readout

887 clock. The measured INL tables that were derived from this calibration were  
888 written into the TDC memory to replace the factory-loaded values. Details on  
889 the procedure and the residual non-linearity affects are given in Ref. [40].

890 The PMT signals are also connected to the FADCs for the pulse charge mea-  
891 surement. The readout employs JLab-designed FADC250 16-channel VME  
892 250 MHz flash ADCs are employed [41]. The JLab-250 FADC units can be  
893 operated in several readout modes. For standard data acquisition operation  
894 the CTOF counters are readout in a mode where the pedestal is subtracted  
895 event-by-event. Fig. 21 shows a raw ADC pulse from a representative CTOF  
896 PMT where the pedestal has been subtracted. Our procedure determines the  
897 pedestal over the first 30 channels. This average is subtracted from our pulse  
898 signal region, which lies between channels 35 and 65. A pulse fitting algorithm  
899 that fits the leading edge of the pulse down to the baseline is used to deter-  
900 mine the hit time from the FADC signal. The readout window for the CTOF  
901 FADCs is set to 192 samples (48 ns). The applied readout threshold is set  
902 to  $\sim 1$  MeV to ensure that the hit cluster energy can be determined with a  
903 reasonable accuracy. Details on the hit clusterization for CTOF are described  
904 in Section 4.2.7. The key performance specifications of these units are given  
905 in Table 6.

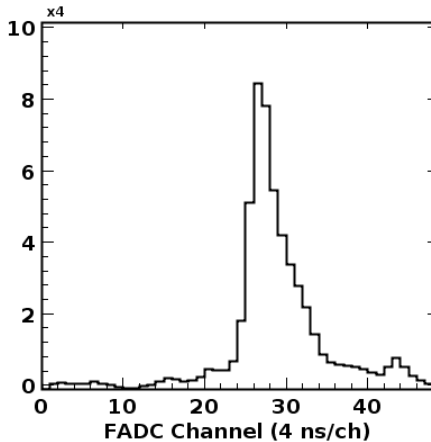


Fig. 21. Average pedestal-subtracted FADC spectrum from a CTOF counter readout from beam data with a 10.6 GeV electron beam incident upon a 5 cm liquid-hydrogen target with the JLab FADC250 module.

906 The PMT anode to splitter panel connections are made using LMR-195 cables,  
907 a low-loss variant of RG-58. LMR-195 is a coaxial cable with a  $50\ \Omega$  charac-  
908 teristic impedance. The upstream PMTs were connected to cable lengths of  
909 15.9 m, 16.3 m, and 16.8 m and the downstream PMTs were connected to  
910 cable lengths of 20.7 m, 21.2 m, and 21.7 m. These cable lengths were re-  
911 quired given the location of the CTOF electronics relative to the PMTs and  
912 were made as short as possible to minimize attenuation and dispersion of the  
913 anode signals. The three different signal cable lengths for the upstream and  
914 downstream PMTs are connected to neighboring PMTs in a repeating cyclical

TDC Specs	ADC Specs
RMS resolution $\leq$ 35 ps	Sampling 250 MHz
Resolution: 21 bit	Resolution: 12-bit
Inter-channel isolation $\leq$ 3 LSB	Clock jitter 350 fs
Double-hit resolution 5 ns	Data memory 8 $\mu$ s
Full-scale range 52 $\mu$ s	Trigger/Data latency 8 $\mu$ s / 32 ns
Integral/Differential non-linearity	
< 2.5 LSB / < 3 LSB	$\pm 0.5$ LSB / $\pm 0.8$ LSB
Inter-channel isolation < 3 LSB	SNR 56.8 dB @ 100 MHz input

Table 6

The key performance specifications of the CTOF CAEN VX1290N pipeline TDCs and JLab FADC250 flash ADCs.

915 pattern. This layout was selected to mitigate the effects of possible counter-  
 916 to-counter cross talk. The signal connections to the ADCs and TDCs were  
 917 also set such that neighboring counters were not connected within the same  
 918 module. The cable connections from the splitters to the readout electronics  
 919 used RG-316 cables of 1.5 m length. RG-316 is a low-loss variant of RG-174.  
 920 RG-316 is a coaxial cable with a  $50 \Omega$  characteristic impedance.

921 The PMTs for the CTOF counters typically operate at about 2000 V with  
 922 negative polarity. The typical dark current drawn by the PMTs on the assem-  
 923 bled counters was < 20 nA. The system is powered by a single CAEN 527  
 924 high voltage mainframe outfitted with negative polarity 24-channel A1535N  
 925 modules that can supply up to 3.5 kV per channel with a maximum current  
 926 of 3 mA. The power supply has a voltage ripple specification of <20 mV  
 927 peak-to-peak (typical). Each channel consumes less than 1 W during counter  
 928 operation. The typical supply currents per channel are 300  $\mu$ A to 500  $\mu$ A.

929 The mainframe is controlled remotely through the Hall B Slow Controls sys-  
 930 tem. A graphical user interface using EPICS [42] running on a UNIX system  
 931 communicates with the mainframe via Ethernet. The mainframe settings en-  
 932 able basic protection of the PMTs in terms of maximum voltage and current  
 933 settings, and channel ramp rates.

934 The high voltage cables for each PMT are fire-retardant RG-59 coaxial cables  
 935 that run from the voltage divider to a local disconnect high voltage (HV)  
 936 distribution box located under the solenoid. There are two 48-channel HV  
 937 distribution boxes for the CTOF. The output of each HV distribution box is  
 938 a pair of 35-ft-long multi-conductor cables, each containing 24-channels, with  
 939 a Radiall connector to mate with the HV A1535N board input connector.  
 940 The multi-conductor high voltage cables employed each contain 30 conductors

941 wrapped in Tefzel insulation, and outer wire shield and PVC insulation wrap.  
942 Each conductor is 5-kV rated.

943 **4 CTOF Performance**

944 This section highlights the performance of the CTOF system both from the  
945 cosmic ray test stand and in Hall B during the first beam runs for CLAS12. The  
946 test stand timing performance is important to understand to ensure that the  
947 performance specifications as detailed in Table 1 are met as the CTOF system  
948 is primarily responsible for the limits of the charged particle identification  
949 separation for CLAS12 in the central direction. Full details on the bench test  
950 performance results for the CTOF counters are provided in Ref. [43].

951 In this section the essential performance results from the bench testing studies  
952 in terms of the counter photoelectron statistics and benchmark timing cali-  
953 brations are presented. Then the nominal algorithms are presented to provide  
954 details on how the in-beam CTOF timing was calibrated and the resolution  
955 quantified. Finally, this section provides the current status of the particle  
956 identification capabilities of the CTOF system in relation to the design spec-  
957 ifications.

958 *4.1 Bench Measurements*

959 *4.1.1 Counter Photoelectron Statistics*

960 The primary approach to determine the number of photoelectrons at the pho-  
961 tocathode of the PMTs generated by minimum-ionizing particles in the scin-  
962 tillation bars employs the ratio of the integral of the pulse for a minimum-  
963 ionizing particle to the integral of the pulse for a single photoelectron. For  
964 these measurements we used the pulse integration feature of an Agilent Tech-  
965 nologies [44] MSO-X 3034A 350 MHz (4 GSa/s) oscilloscope and averaged  
966 1000 pulses. The minimum-ionizing particle signals were analyzed connecting  
967 the scope to the PMT when mounted in position on the CTOF counter. For  
968 the single photoelectron signal, we took data using just a bare PMT on the  
969 bench using the same gain setting. For both measurements the oscilloscope  
970 threshold was adjusted appropriately. For the minimum-ionizing peak analy-  
971 sis the threshold had to be set high enough ( $>200$  mV) to eliminate tracks  
972 that did not pass normally through the bar. For the single photoelectron peak  
973 the threshold had to be set low enough (1 mV) to pick out the noise pulses  
974 that were the source of the PMT intrinsic dark current. This measurement  
975 scheme yielded 200 photoelectrons per MeV of deposited energy at a gain of

976  $1 \times 10^6$ , which corresponds to  $\sim 0.03$  nC/MeV.

977 *4.1.2 Bench Time Resolution Performance*

978 The basic algorithm used on the test bench for the CTOF counters to deter-  
 979 mine the time resolution of a given reference counter was to use incident cosmic  
 980 ray muon tracks to compare the measured time for the reference counter to  
 981 the time measured by two other identical counters in a triplet counter con-  
 982 figuration (see Fig. 22). For a triplet measurement, where the track passes  
 983 through all three counters with double-sided readout, six times are measured  
 984 ( $t_1 \rightarrow t_6$ ). Each time measurement actually represents the difference between  
 985 the discriminated PMT signal (TDC start) and the trigger time (TDC stop  
 986 from the six PMT coincidence). These timing measurements are then trans-  
 987 lated into three counter hit times  $t_{t,m,b} = \frac{1}{2}(t_{1,3,5} + t_{2,4,6})$ .

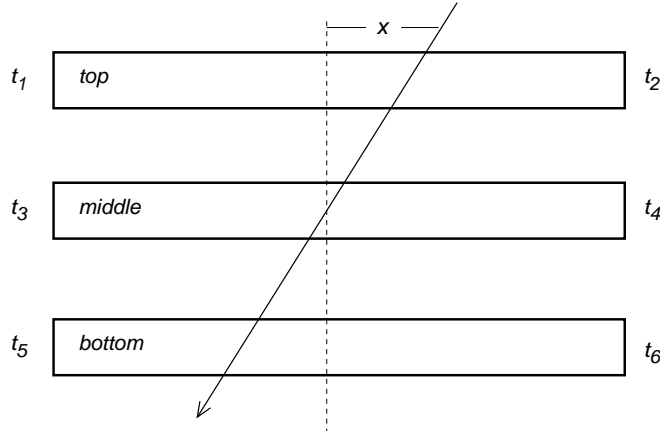


Fig. 22. Schematic representation of a triplet of counters (labeled top -  $t$ , middle -  $m$ , bottom -  $b$ ) with a muon track traversing the stack. The geometry of the triplet is configured such that the separation between the top and middle counters matches that of the middle and bottom counters.

988 For incident tracks that pass fully through each counter of the triplet with  
 989 measured times  $t_t$ ,  $t_m$ , and  $t_b$ , we can define a time residual  $t_r = t_m - \frac{1}{2}(t_t +$   
 990  $t_b)$ , where we should expect that the time  $t_m$  of the middle scintillator hit  
 991 should be the average of the measured times  $t_t$  and  $t_b$  for the top and bottom  
 992 scintillators, respectively. Thus the measured residual  $t_r$  should nominally  
 993 be 0. However, due to the smearing of the measured times  $t_t$ ,  $t_m$ , and  $t_b$  due  
 994 to the finite time resolution of the measurements, the residual time  $t_r$  will also  
 995 be smeared. While we still expect the mean of  $t_r$  to be zero, the width of the  
 996  $t_r$  distribution can be used to determine the average time resolution of each  
 997 counter in the triplet. (For the outer counters in the triplet, the definition  
 998 of the time residual must be slightly modified to account for the small path  
 999 length difference between the reference counter and the other two counters.)

1000 The average time resolution of each counter is computed from the variance  
 1001  $\delta t_r$  in the measured time residual  $t_r$ . Assuming the average time resolution  
 1002 for each PMT in the triplet ( $\Delta t_i, i = 1 \rightarrow 6$ ) is identical and taking into  
 1003 account that each counter is readout using two PMTs, we can write the final  
 1004 expression for the average counter timing resolution as:

$$1005 \quad \sigma_{counter} = \frac{2}{\sqrt{6}} \delta t_r. \quad (6)$$

1006 Thus a measure of the width ( $\sigma$ ) of the time residual distribution provides a  
 1007 measure of the average resolution of each counter in the triplet.

1008 *4.1.3 Bench Measurement Counter Timing Resolutions*

1009 Fig. 23 shows the average timing resolution measured for each CTOF counter  
 1010 using the triplet counter configuration. This analysis included a minimum  
 1011 ADC cut to remove events with low photon statistics that did not pass through  
 1012 the full width of the counter and also a coordinate cut of  $\pm 10$  cm about the  
 1013 center of the scintillation bar. Here the average counter timing resolution is  
 1014 roughly 70 ps. The resolution on average is slightly worse for the top and  
 1015 bottom counters of each cart due to the uncertainties in the path length cor-  
 1016 rections discussed in Section 4.1.2. Given the discussion of the time resolution  
 1017 measurement limitations in Section 4.1.4, these results are quite encouraging  
 1018 compared to the design specifications.

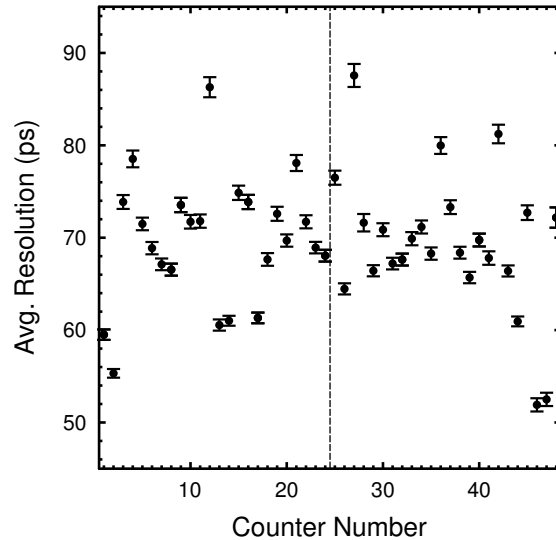


Fig. 23. Measured average CTOF counter resolution with a cut on the measured  
 ADC values and a cut on the measured hit coordinates to select events going through  
 the middle of the counter. The vertical line separates the low-pitch angle counters  
 (#1 to #24) from the high-pitch angle counters (#25 to #48).

1019 The CTOF counter time resolutions were studied vs. three independent vari-  
 1020 ables: track coordinate, ADC geometric mean, and track angle. Table 7 shows  
 1021 details on the variable ranges and bin sizes used for these studies. The bin sizes  
 1022 were selected to achieve reasonable statistical precision in the measurements  
 1023 given the limited statistics for the week-long data run.

Quantity	$N_{bins}$	Lower Limit	Upper Limit	Bin Size
Track Coordinate	16	-40 cm	40 cm	5 cm
ADC Geometric Mean	16	1250	6050	300 channels
Track Angle	16	-45°	45°	5.625°

Table 7

Details on the limits and bin sizes selected for the counter timing resolution studies vs. track coordinate, ADC geometric mean, and track angle.

1024 Fig 24 shows the average resolution for a representative CTOF counter as a  
 1025 function of hit coordinate, ADC value, and track incidence angle. The res-  
 1026 olution is optimal about the center of the counter and gets worse near the  
 1027 ends where one PMT receives its minimum light due to attenuation length  
 1028 effects. The resolution is reasonably flat over the ADC range corresponding  
 1029 to muons more or less normally incident upon the counters (channel 2000 for  
 1030 these studies). There is a slight improvement with higher ADC values as more  
 1031 light reaches the PMTs. As the resolution is proportional to photo-statistics,  
 1032 the larger the energy deposited the better the timing resolution. The res-  
 1033 olution improves with increasing angle due to a correspondingly longer path  
 1034 through the scintillation material that results in increased photo-statistics.

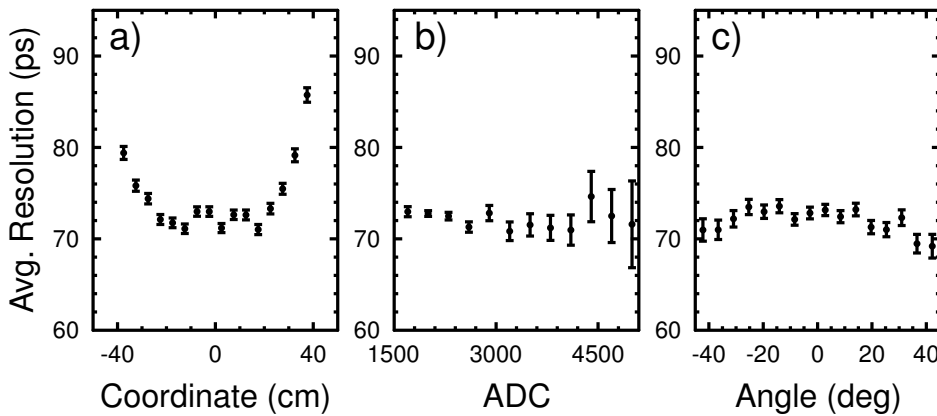


Fig. 24. Dependence of the counter time resolution for a representative counter on a). the coordinate of the reference counter, b). the average reference counter ADC value, and c). the angle of incidence of the track.

1035 One final note to mention here with regard to the bench test time counter  
 1036 resolution measurements is that a series of studies were carried out replacing  
 1037 the constant fraction discriminators (CFDs) with leading edge discriminators  
 1038 (LEDs). The timing resolution results using LED readout including appropri-

1039 ate off-line time-walk corrections were consistent with those using the CFDs  
1040 that do not require the time-walk corrections. These results are detailed in a  
1041 separate report [45].

1042 *4.1.4 Limitations to Bench Measurements*

1043 There are two factors involved in the bench test studies that limited the accuracy  
1044 of the measured CTOF counter time resolutions. The first arose from the extremely low data rate for each triplet of counters ( $< 0.1$  Hz) due to the narrow counter width and the counter-to-counter separation of  $\sim 21.6$  cm. Data  
1045 runs of  $\sim 1$  week were necessary to collect sufficient statistics to determine  
1046 the counter resolutions. Due to the inherent calibration drifts over this time  
1047 that could not be tracked precisely, the measured counter time resolutions  
1048 were smeared. The second factor arose due to the counter-to-counter alignment  
1049 within the carts was only at the level of  $\pm 0.64$  cm. This scale was set  
1050 by the fairly crude design of the carts and the counter supports, which were  
1051 mainly intended for counter assembly, wrapping, and storage. With counter-to-  
1052 counter separations of  $\sim 21.6$  cm, the inaccuracies of the alignment were such  
1053 that the residual centroids were correlated with the hit coordinates, which  
1054 again smeared the counter time resolutions. The contributions of both factors  
1055 smeared the measured time resolutions by 10% to 20%.

1058 *4.2 CTOF Beam-Data Calibrations*

1059 In the nominal data taking mode for CLAS12, whenever the CTOF is involved  
1060 in an event that triggers the spectrometer, the ADCs and TDCs for all PMTs  
1061 with a signal above the discriminator threshold are recorded. For the FADCs,  
1062 the charge of the pulse is integrated over the extent of the pulse region and  
1063 the pedestal is subtracted event by event as discussed in Section 3.8. For the  
1064 TDCs the time recorded is relative to the trigger. To determine the flight time  
1065 of the charged track from the target to the CTOF, the TDC time must be  
1066 compared to the time of the accelerator radio frequency (RF) pulse relative to  
1067 the trigger. The RF signal from the accelerator has a period an integer multiple  
1068 of 2.004 ns. The RF bunch length itself corresponds to a few picoseconds.  
1069 Although the timing signals are very accurate (with a resolution of  $< 20$  ps),  
1070 the determination of which beam bunch produced a given interaction must be  
1071 determined by the experiment.

1072 The full energy and timing calibration of the each of the CTOF counters  
1073 involves a number of discrete steps. The calibration constants for each run are  
1074 stored in the CLAS12 calibration database. The calibrations are monitored for  
1075 each data run (which lasts typically for 2 hrs) and redone only when there are

1076 shifts in the response outside of established ranges (which are typically 5%).  
1077 The steps to the CTOF calibration are carried out in a particular as detailed  
1078 in Ref. [46] and highlighted below.

- 1079 (1) ADC Calibration: Determine the ADC channel to energy deposition cal-  
1080ibration factor for each counter using minimum-ionizing events. See Sec-  
1081tion 4.2.1.
- 1082 (2) Upstream/downstream PMT time offsets: This time offset accounts for  
1083 the difference in the time recorded between the upstream and down-  
1084 stream PMTs in a given counter due mainly to the different signal cable  
1085 lengths used for the connection to the readout electronics. These time  
1086 offsets are determined from the centroid of the difference between the  
1087 upstream/downstream TDC time difference and the computed track hit  
1088 coordinated divided by the effective speed of light in the counter.
- 1089 (3) Attenuation Length Calibration: This property of the counter quantifies  
1090 the light absorption length and is determined by relating the measured  
1091 ADC as a function of hit coordinate along the bar. See Section 4.2.2.
- 1092 (4) Effective Velocity Calibration: Determine the effective speed of light prop-  
1093 agation along the counter. See Section 4.2.3.
- 1094 (5) Counter-to-Counter Time Offset Calibration: In order to measure the  
1095 absolute flight time of a charged particle from the target to the CTOF  
1096 counter and to be able to reconstruct exclusive events when hits are  
1097 associated with multiple CTOF counters, the relative time offsets of each  
1098 counter relative to all of the other counters in the system need to be  
1099 determined. This is done in two steps. The first step is to align each track  
1100 to the RF time, a step that amounts to a precision time alignment in bins  
1101 of the TDC LSB. The second step is a coarse alignment of each counter  
1102 time in bins of the RF period  $T_{RF}$ . See Section 4.2.4. During this step  
1103 the effective counter timing resolutions are extracted (see Section 4.2.6).
- 1104 (6) TDC Calibration: After calibrating the integral non-linearities of each  
1105 TDC channel in the system (see Section 3.8), the TDC channel to time  
1106 calibration is completed using beam events. See Section 4.2.5.

#### 1107 4.2.1 Gain Matching

1108 One of the purposes of gain-matching the CTOF PMTs is to equalize the  
1109 detector response to tracks that cross the CTOF barrel such that two coun-  
1110 ters are involved. This is a necessary procedure because each counter must  
1111 contribute equally to the trigger for a common-threshold discriminator level.  
1112 Gain matching so that the minimum-ionizing particle peak appears in the  
1113 same ADC channel for all counters also allows for easier data monitoring dur-  
1114 ing online and offline analysis.

1115 The CTOF PMT high voltage settings were determined using calibration runs

employing minimum-ionizing tracks. These minimum-ionizing tracks deposit roughly 6 MeV as they pass through the 3 cm thick CTOF scintillation bars, as  $dE/d\rho x = 1.956 \text{ MeV/g/cm}^2$  for minimum-ionizing particles. The initial high voltage settings were based on runs using cosmic ray muons with the solenoid at zero field with the readout based on a trigger that required tracks to cross the barrel to select tracks approximately normal to the face of the CTOF counters. During production data taking, these calibrations are carried out using minimum-ionizing tracks from beam data coming from the target. In this case the charge information is scaled by a path length correction given by  $t/P$ , where  $t$  is the counter thickness and  $P$  is the path-length of the track in the counter as determined by extrapolation of the track beyond the central tracker to the location of the CTOF counter.

The energy deposited in the scintillation bars follows a Landau distribution for the minimum-ionizing tracks. The energy deposited is recorded by the ADCs, which show a peak above pedestal for the tracks. Tracks that do not pass through the full counter thickness and non-minimum-ionizing tracks give rise to a background beneath the Landau peak.

For the HV calibrations, to avoid issues with the attenuation of light for tracks that pass near the ends of the bars and to avoid issues with unbalanced light entering the upstream and downstream PMTs, we combine the pedestal-subtracted ADC information from the upstream and downstream PMTs to produce an average ADC spectrum for the counter through the quantity known as the ADC geometric mean given by:

$$\overline{ADC} = \sqrt{(ADC - PED)_U \cdot (ADC - PED)_D}. \quad (7)$$

Fig. 25 shows the geometric mean spectrum for one representative CTOF counter using beam data.

Given the finite dynamic range of the ADC, we have chosen to position the minimum-ionizing muon peak in a particular ADC channel that is selected so that it is safely above the pedestal, but leaves sufficient range for the more highly ionizing charged tracks of our typical physics events. To minimize PMT aging effects that result in loss of PMT gain with time correlated with the total charge collected at the first dynode of the accelerating structure, the PMT gains are set as low as possible.

The PMT gains depend exponentially on the applied voltage. Expressed in a slightly different way, we can relate the PMT gain  $G_1$  at a given voltage  $V_1$  to the gain  $G_2$  at a different voltage  $V_2$  via:

$$\frac{G_1}{G_2} = \left( \frac{V_1}{V_2} \right)^\alpha. \quad (8)$$

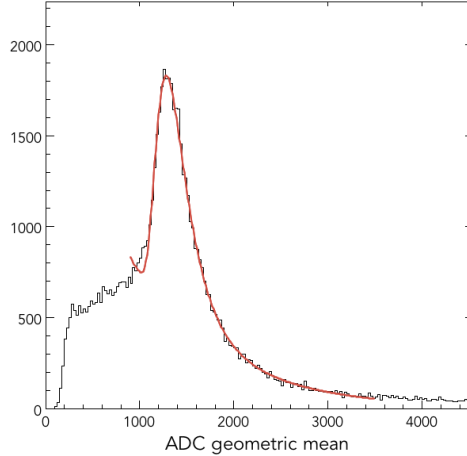


Fig. 25. (Color Online) Geometric ADC mean for one representative CTOF counter from beam data in CLAS12. The events recorded in the ADC spectrum have been pedestal subtracted. The red curve is the fit function that includes a Landau shape for the peak and an exponential for the background.

1153 This is a basic power law form with  $\alpha$  representing the power law factor.  
 1154 Rewriting Eq.(8) in a slightly different form, we have:

$$1155 \quad \frac{\Delta G}{G} = \alpha \frac{\Delta V}{V}. \quad (9)$$

1156 It is this expression that is the basis for relating the position of the muon  
 1157 peak in the  $\overline{ADC}$  spectrum (see Eq.(7)) to the PMT HV setting. The gain-  
 1158 matching procedure then amounts to adjusting the HV settings of all PMTs to  
 1159 the values required to position the muon peak for each counter in the desired  
 1160 ADC location. At the same time the algorithm uses the individual upstream  
 1161 and downstream PMT ADC spectra for a given counter to ensure that these  
 1162 PMT gains are balanced.

1163 The iterative process to determine the final set of PMT HV values typically  
 1164 converges in 1 to 2 data runs. For initial operation of the PMTs we have chose  
 1165 to center the muon peak in the  $\overline{ADC}$  spectrum for each counter in channel  
 1166 900. At the typical PMT voltage settings of  $-1500 \rightarrow -2000$  V, the HV supply  
 1167 currents for each channel are in the range from  $300 \mu\text{A}$  to  $500 \mu\text{A}$ .

1168 The determination of the power law factor  $\alpha$  in Eq.(8) is important in order  
 1169 for the HV calibrations to converge quickly. This factor can be determined  
 1170 directly from the data. For this purpose, two data runs were acquired with  
 1171 different HV settings for the PMTs. After determining the locations of the  
 1172 muon peaks from the ADC spectrum fits, Eq.(9) was used to solve for  $\alpha$  for  
 1173 all PMTs. The average value from the data was determined to be  $\alpha=4$  as  
 1174 shown in Fig. 26.

1175 The energy loss in a counter for a passing charged particle track is determined

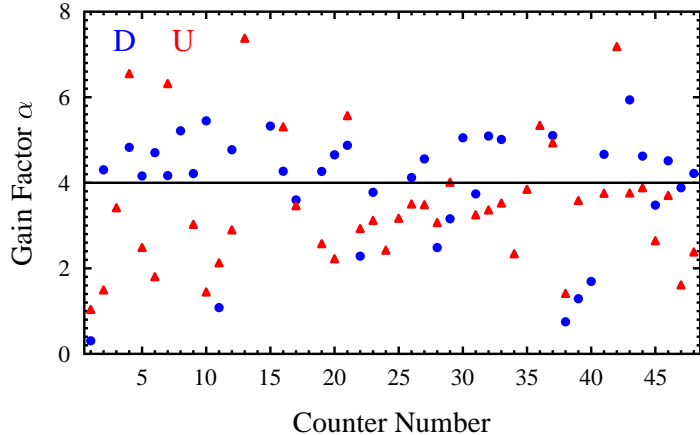


Fig. 26. (Color Online) Data showing the measurements of the power law factor  $\alpha$  for each CTOF upstream PMT (red triangles) and downstream PMT (blue circles). The average values of  $\alpha$  for the CTOF PMTs is 4.

1176 after the minimum-ionizing peak centroids are aligned. The computed energy  
 1177 loss in each counter is computed from each PMT as:

$$1178 \quad E_{U,D} = ADC_{U,D} \cdot \left[ \frac{\left( \frac{dE}{dx} \right)_{MIP} \cdot t}{ADC_{MIP}} \right] \exp \left( \frac{d_{U,D}}{\lambda} \right), \quad (10)$$

1179 where  $ADC_{MIP}$  is the centroid of the minimum-ionizing peak in the geometric  
 1180 mean distribution,  $\left( \frac{dE}{dx} \right)_{MIP}$  is the energy loss for minimum-ionizing particles  
 1181 in the scintillation bars (1.956 MeV/cm),  $t$  is the counter thickness,  $d$  is the  
 1182 distance along the bar from the track hit position to the PMT, and  $\lambda$  is the  
 1183 counter attenuation length. The energy loss used in the event reconstruction  
 1184 is the mean of the separate  $E_{U,D}$  measures.

1185 Fig. 27 shows the reconstructed energy loss normalized by the track path  
 1186 length summed over all counters from a data run with a 10.6 GeV elec-  
 1187 tron incident upon a liquid-hydrogen target. The data allow the separation of  
 1188 minimum-ionizing particles from more heavy ionizing particles. The minimum-  
 1189 ionizing particles lose a constant energy as a function of path length. The heav-  
 1190 ily ionizing particles have energy loss that increases linearly with distance at  
 1191 low momentum until they can pass through the counter. At that point their  
 1192 energy loss follows the Bethe-Bloch formula.

#### 1193 4.2.2 Attenuation Length Measurements

1194 The attenuation length of the scintillation bars represents the distance  $\lambda$  into  
 1195 the material where the probability that the photon has been absorbed is  $1/e$ .  
 1196 For the scintillation bars, as more collected light translates into better timing  
 1197 resolution, it is important for the attenuation length to be as long as possible.

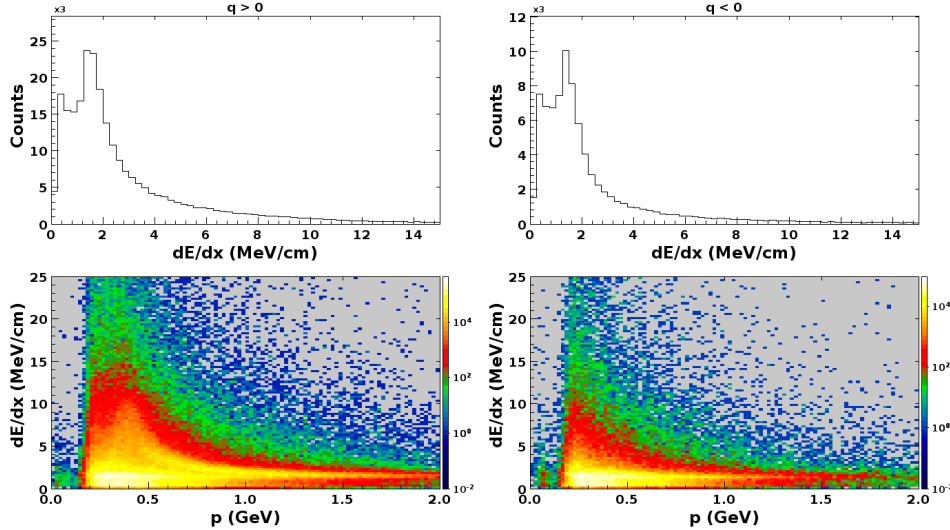


Fig. 27. (Color Online) Measured CTOF counter energy loss summed over all counters for positively charged particles (left column) and negatively charged particles (right column) from 10.6 GeV electrons incident on a liquid-hydrogen target normalized by the extrapolated path length from the projection of the central track through the CTOF barrel. These  $dE/dx$  (MeV/cm) plots show separation of minimum-ionizing particles from more heavily ionizing particles. The top row of plots show the measured  $dE/dx$  and the bottom row of plots show  $dE/dx$  vs. track momentum (GeV).

1198 The general design goal was that the attenuation length be on the order of  
 1199 the overall length of the bars.

1200 For EJ-200, this bulk attenuation length is reported by the manufacturer as  
 1201 380 cm [47]. The practical attenuation length of the scintillation material turns  
 1202 out to be about half the bulk attenuation length. The coupling of the CTOF  
 1203 scintillation bars to the Acrylic light guides reduces the measured counter prac-  
 1204 tical attenuation length by another  $\sim 35\%$  to 50% (corresponding to  $e^{-L_{LG}/\lambda_A}$ ,  
 1205 where  $L_{LG}$  is the light guide length and  $\lambda_A=2.3$  m (see Section 3.3.2)).

1206 The measured ADC values for each PMT can be written in terms of the  
 1207 attenuation length as:

$$1208 \quad ADC_{U,D} = A_0^{U,D} e^{\pm x/\lambda}, \quad (11)$$

1209 where  $A_0^U$  and  $A_0^D$  are constants and  $\lambda$  is the counter attenuation length. Then,

$$1210 \quad \log \left( \frac{(ADC - PED)_U}{(ADC - PED)_D} \right) = C + \frac{2x}{\lambda}, \quad (12)$$

1211 and a linear fit of the ADC log ratio vs. coordinate  $x$  is used to extract the  
 1212 effective counter attenuation length. Here the hit coordinate along the counter

1213 is determined using the measured TDC hit times  $t_U$  and  $t_D$  from:

1214

$$x = (t_U - t_D) \cdot \frac{v_{eff}}{2}, \quad (13)$$

1215 where  $v_{eff}$  is the effective velocity of light in the scintillation counter. Note  
 1216 that the PMT transit time and signal cable propagation times are taken out  
 1217 to center the coordinate distribution about zero. Fig. 28 shows the measured  
 1218 average attenuation lengths for the CTOF counters. The average attenuation  
 1219 length is found to be 140 cm in accord with expectations.

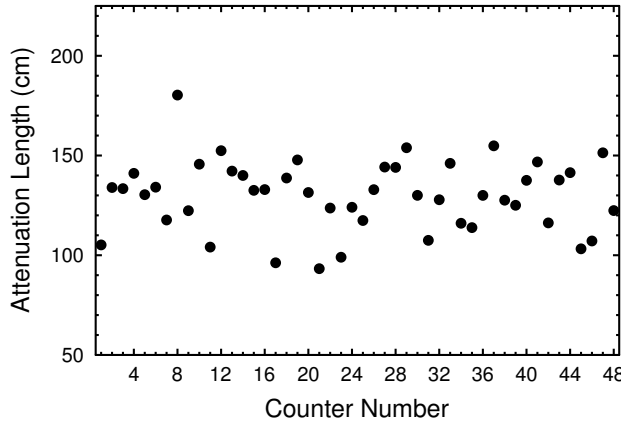


Fig. 28. Counter attenuation lengths (cm) vs. counter number determined from beam data.

1220 *4.2.3 Effective Velocity Determination*

1221 The effective velocity of light in each counter employs a calculation based com-  
 1222 paring the reconstructed coordinate information along the scintillation bar  
 1223 from the timing information and from the track hit coordinate determined  
 1224 from extrapolation of the track beyond the central vertex tracker to the loca-  
 1225 tion of the CTOF counters. Fig. 29 shows the measured effective velocity for  
 1226 each CTOF counter using data with a 10.6 GeV electron beam incident on a  
 1227 liquid-hydrogen target.

1228 *4.2.4 Counter-to-Counter Time Alignment*

1229 The flight time of a charged particle from the reaction vertex to a CTOF  
 1230 counter is given by:

1231

$$TOF = \bar{t}_{hit} - t_{ST}, \quad (14)$$

1232 where  $\bar{t}_{hit}$  is the average CTOF counter hit time (using  $t_U$  and  $t_D$ ) and  $t_{ST}$  is  
 1233 the event start time. The event start time is associated with the RF but needs

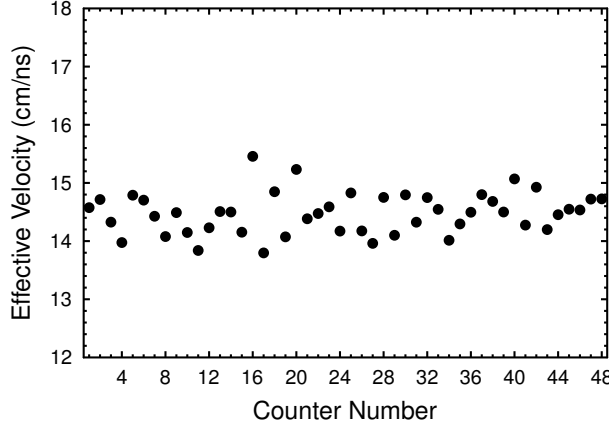


Fig. 29. Counter effective velocities (cm/ns) vs. counter number determined from beam data.

to be synchronized with the particular RF beam bucket associated with the event. The beam bunch width within the RF beam bucket is only  $\sim 2$  ps and, therefore, represents a precise time marker. However, as the RF time signal has a period of  $T_{RF}$ , it is not initially known which RF beam bucket was the one associated with the event that led to the hits in the CTOF counter.

The determination of the absolute flight time of charged particle tracks from the reaction vertex to the CTOF counters is performed in two steps. In the first step, fine timing offsets (binned in the LSB of the TDCs = 25 ps) are determined to align the CTOF hit times traced back to the vertex for each counter within the RF time window. In the second step, coarse timing offsets binned in units of the RF period  $T_{RF}$  are determined to fix the specific RF beam bucket associated with the event.

The fine timing alignment algorithm uses the CTOF hit time traced to the event vertex relative to the RF to align the vertex times of all CTOF hits (modulo  $T_{RF}$ ). This algorithm uses the average counter hit times,

$$t'_{res} = \text{mod} \left[ \left( \left( \bar{t}_{hit} - \frac{L}{\beta c} \right) - \left( t_{RF} + \frac{z_{vert}}{\beta_e c} \right) \right), T_{RF} \right]. \quad (15)$$

The term  $z_{vert}/(\beta_e c)$  is a term to correct the RF time  $t_{RF}$  to account for the actual electron beam event vertex location along the  $z$ -axis of the extended target (hence the use of  $\beta = \beta_e$ ).

Fig. 30 shows the  $t'_{res}$  distribution for one representative CTOF counter. The centroid of the Gaussian fit gives the fine timing offset. The width of the Gaussian fit represents a measure of the effective timing resolution of the counter. To display the full  $t'_{res}$  distribution avoiding any wrap-around effects near the edges of the  $T_{RF}$  range, the algorithm plots the  $t'_{res}$  distribution in a range of  $\pm T_{RF}/2$  about the peak channel in the distribution.

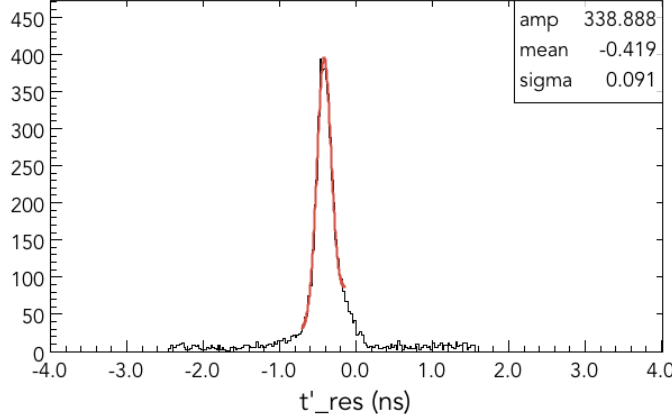


Fig. 30. (Color Online) Distribution of the CTOF hit times from beam data traced back to the vertex relative to the RF (ns) for one representative CTOF counter with the Gaussian plus background fit overlaid to determine the counter RF offset and the effective counter timing resolution.

After the fine timing offset calibration, the counter timing is precisely aligned modulo  $T_{RF}$ . The next step in the CTOF timing calibration is to fix the measured hit times for all counters to the specific RF bunch associated with the event. These coarse timing offsets (called P2P for paddle-to-paddle) are determined using coincidences of charged particle tracks with one track in the forward direction hitting an FTOF counter and one track in the central detector hitting a CTOF counter. The offsets for each counter are computed using the time difference:

$$t_{P2P} = t_{vert}^1 - t_{ST}^2, \quad (16)$$

where,

$$t_{vert}^i = \bar{t}_{hit}^i - \frac{L}{\beta c}. \quad (17)$$

Here  $t_{ST}$  is the event start time determined using the forward-scattered electron each event. The event start time is determined using the Forward Time-of-Flight system. Therefore the CTOF timing calibrations can proceed only after the FTOF timing calibrations have been completed. The algorithm adjusts the vertex time differences over all counters to set them to zero. The coarse time offsets represents a single parameter for each counter that is restricted to values of  $n \cdot T_{RF}$ , with  $n = 0, \pm 1, \pm 2, \dots$ .

Fig. 31 shows the  $t_{P2P}$  distribution for one representative CTOF counter. As expected, the histogram is dominated by events in a single channel (of width  $T_{RF}$ ) centered about  $T_{RF} = 0$ . As these constants are predominantly determined by the fixed system cable lengths, the constants primarily reflect the differences in the signal propagation times along the signal cables.

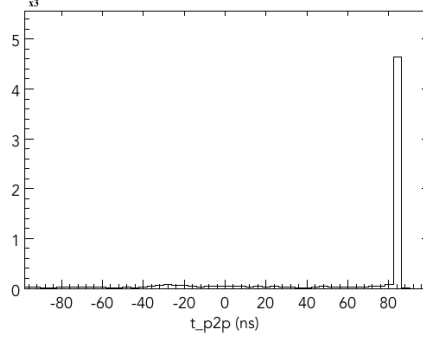


Fig. 31. Distribution of the vertex time differences (ns) for tracks in a single representative CTOF counter compared to the event start time determine from the FTOF system. As this plot has been made after the timing calibrations of the FTOF system have been completed, the dominant bin in this distribution at 80 ns, gives the P2P offset for this CTOF counter. The histogram is sorted in bins of  $T_{RF}$ .

#### 1282 4.2.5 TDC Calibration

1283 The final calibration step is the calibration of the TDCs. This calibration is a  
 1284 single constant for each TDC channel in the system that converts the measured  
 1285 TDC channel bin into time. The nominal TDC LSB is 25 ps for the CAEN  
 1286 VX1290N TDC units employed for the CTOF readout (see Section 3.8).

1287 The calibration is completed by fitting the PMT time residuals vs. TDC chan-  
 1288 nel separately for the times from the upstream and downstream PMTs using  
 1289 a linear function. The TDC calibration is the value that fixes the slope of  
 1290  $t'_{res}$  to be zero. Fig. 32 shows the distribution of  $t'_{res}$  vs. TDC for a represen-  
 1291 tative CTOF PMT. Any bin-to-bin  $\Delta t$  variations reflect remaining integral  
 1292 non-linearities in the measured TDC compensation tables (see Section 3.8).  
 1293 At the present time a single conversion constant of CONV = 23.45 ps/channel  
 1294 is employed for the CTOF system TDCs.

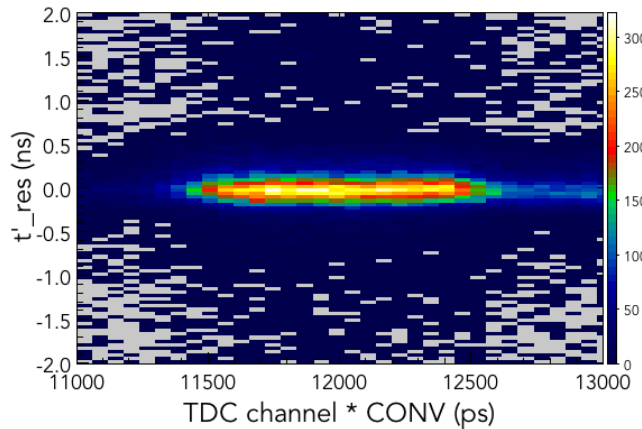


Fig. 32. (Color Online) Distribution of  $t'_{res}$  (ns) vs. TDC channel \* CONV (ps) for one representative CTOF PMT. The TDC conversion constant for each channel is that which forces the slope of a linear fit to be zero.

1295 The CAEN TDCs used for the CTOF are readout with a 24 ns clock strobed

1296 so that all TDC times are referenced to an edge of this clock. The CLAS12  
1297 trigger comes on the edge of a clock with a period of 4 ns and the TDC stop  
1298 will not occur until the next 24 ns clock edge. The use of these two different  
1299 clocks introduces a delay between the trigger and the TDC stop given by  
1300  $n \cdot 4$  ns, with  $n = 0 \rightarrow 5$  (referred to as the six-fold TDC cycle ambiguity)  
1301 where  $n$  is the phase. A TDC jitter correction is made to define the value of  
1302 the phase  $n$  that is valid for the entire data run.

1303 The average hit time resolution for the CTOF from the TDCs is  $\sim 70$  ps and  
1304 that from the CTOF FADCs given the rapid fall time of the fast PMT signals  
1305 that provide for only 2-3 samples on the falling edge is only  $\sim 1$  ns. A matching  
1306 requirement of 10 ns between the TDC time and the FADC time is employed  
1307 during event reconstruction. While this matching requirement still needs to  
1308 be tuned further, at the current time is reasonably efficient at allowing the  
1309 FADC hits to be matched with the TDC hits. This is important as due to  
1310 the different thresholds on the discriminators and the FADCs, the number of  
1311 entries in the hits lists are up to a factor of two different. The matching criteria  
1312 is also essential in order to assign the correct ADC information to the hit that  
1313 directly uses the measured ADC but also for the energy loss computation.

#### 1314 4.2.6 Counter Time Resolutions

1315 The effective time resolutions for each counter determined during the fine  
1316 timing alignment step discussed in Section 4.2.4 are shown in Fig. 33. These  
1317 measurements were taken after complete calibrations of the CTOF system  
1318 from a beam data run with 10.6 GeV electrons incident on a liquid-hydrogen  
1319 target. The time resolution displayed here represents the quality of the overall  
1320 CLAS12 calibrations at the current time. The results are based on calibration  
1321 procedures that are not yet fully optimized, as well as uncertainties in  
1322 the momentum, track path length, and event vertex from the forward and  
1323 central track reconstruction. It is also important to mention that studies of  
1324 the CLAS12 subsystem detector alignment based on survey data and based on  
1325 zero-field straight track data are in progress. Misalignments of the detector af-  
1326 fect the quality and accuracy of the reconstruction. When these are accounted  
1327 for their contribution to the resolution function is reduced.

1328 Nevertheless the time resolutions already achieved are close to system design  
1329 specifications outlined in Section 2 and shown in Table 1. With these reso-  
1330 lutions, the quality of the particle identification in the Central Detector of  
1331 CLAS12 allows the experimental program in Hall B to reach its goals. As fur-  
1332 ther operating experience with CLAS12 is gained, we expect to realize further  
1333 modest but important improvements in the CTOF timing resolution that will  
1334 allow  $\pi/K$ ,  $\pi/p$ , and  $K/p$  separation in the Central Detector of CLAS12 to  
1335 be pushed to higher momenta than currently seen.

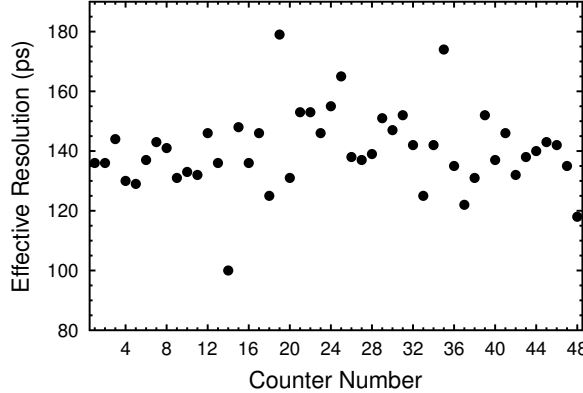


Fig. 33. The measured effective time resolution (ps) vs. counter number for each of the CTOF counters from beam data for a 10.6 GeV electron beam incident upon a liquid-hydrogen target.

1336 Note that as discussed in the Section 3 introduction, the final CTOF counter  
 1337 resolutions shown in Fig. 33 are listed as effective timing resolutions as they  
 1338 include additional smearing effects beyond that included in the resolutions  
 1339 discussed and shown in Section 4.1.2 determined from the cosmic ray test  
 1340 stand. The contributions from all non-CTOF sources to the effective resolution  
 1341 effectively adds  $\sim 50$  ps of smearing in quadrature with the intrinsic CTOF  
 1342 system resolution.

#### 1343 4.2.7 Hit Times and Clusterization

1344 The reconstructed CTOF counter hit times need to account for the time de-  
 1345lays along the readout path that include the PMT and voltage divider signal  
 1346 transit times, and the signal propagation times along the signal cables and  
 1347 the electronics. Full details on the CTOF reconstruction in terms of recon-  
 1348structed hit times and energy, the reconstruction algorithm, the time, energy,  
 1349 and coordinate uncertainties, and the hit clustering and matching algorithms  
 1350 are provided in Ref. [48].

1351 The track hit times reconstructed from the readout of the upstream and down-  
 1352 stream PMTs are given by:

$$1353 t_{U,D} = (CONV \cdot TDC_{U,D}) \mp \frac{C_{UD}}{2} + C_{RF} + C_{p2p}, \quad (18)$$

1354 where  $CONV$  is the TDC channel to time conversion factor,  $TDC$  is the  
 1355 measured TDC value relative to the trigger signal,  $C_{UD}$  is the time shift to  
 1356 center the TDC difference distribution relative to the track coordinate about  
 1357 0, and  $C_{RF}$  and  $C_{p2p}$  are the time shifts to align all of the counter times with  
 1358 respect to the RF and to each other, respectively.

1359 The hit times of the passing charged particle relative to the trigger signal can  
 1360 be determined separately from the times  $t_U$  and  $t_D$  measured by the upstream  
 1361 and downstream PMTs, respectively, and are given by:

$$1362 \quad t_{hit}^{U,D} = t_{U,D} - \frac{d_{U,D}^{CVT}}{v_{eff}}, \quad (19)$$

1363 where  $d_{U,D}^{CVT}$  are the distances from the track hit point along the bar relative  
 1364 to the end of the bar as determined by the central tracker. The average CTOF  
 1365 hit time is then given by:

$$1366 \quad \bar{t}_{hit} = \frac{1}{2}(t_{hit}^U + t_{hit}^D) = \frac{1}{2} \left[ t_U + t_D - \frac{L}{v_{eff}} \right]. \quad (20)$$

1367 The output from the FADCs is also used as part of the CLAS12 level-1 trigger.  
 1368 Signals in CTOF above the FADC threshold of  $\sim 1$  MeV are used to set a trig-  
 1369 ger bit that defines charged hadrons in the CLAS12 Central Detector. Signals  
 1370 from the CTOF system are also used to provide an effective charged particle  
 1371 veto for the detection of neutrals in the neutron detector radially outward  
 1372 from CTOF. While high resolution timing measurements are the primary role  
 1373 of the CTOF system for charged particle identification in the central direction  
 1374 of CLAS12, the pulse height information from the FADCs is also employed for  
 1375 energy loss measurements to provide an independent means for identification  
 1376 of slow particles. In addition, pulse fitting techniques are employed using the  
 1377 FADC pulse shape to determine the hit time of the track that is matched to  
 1378 the TDC time to better ensure matching of the ADC and TDC information  
 1379 in the high rate operating environment of CLAS12.

1380 Particle trajectories from the target passing through the CTOF barrel can  
 1381 pass through up to two adjacent counters. To determine the full deposited  
 1382 energy in a given counter layer, a clusterization algorithm is used to match  
 1383 the CTOF counter hits with the track trajectory at the location of the CTOF  
 1384 array. Neighboring CTOF hits that match to the trajectory are assigned to be  
 1385 part of a cluster. The assigned cluster energy is then the sum of the deposited  
 1386 energy in both counters,

$$1387 \quad E_{cluster} = \sum_{i=1}^2 E_{dep}^i. \quad (21)$$

1388 The relevant path length through the layer is then determined from ray tracing  
 1389 of the central tracker in the solenoid field. This path length through the CTOF  
 1390 is then used to compute  $dE/dx$ .

1391 The hit time associated with the cluster in a given layer is based on an energy

1392 deposition weighted average accounting for the time offset between the cluster  
 1393 hits. For the CTOF reconstruction the assigned hit position in the counter is  
 1394 based on ray tracing of the charged track through the CTOF barrel. For each  
 1395 counter the hit position is assigned as mid-way between the track entrance  
 1396 point and exit point on the bar. In this way a cluster hit time is computed as:

$$1397 \quad t_{hit} = t_i \cdot \frac{E_i}{E_{cluster}} + \left( t_{i+1} - \frac{\Delta r_C}{\beta c} \right) \cdot \frac{E_{i+1}}{E_{cluster}}, \quad (22)$$

1398 where  $\beta c$  is the track speed,  $\Delta r_C$  is the distance between the hit positions  
 1399 assigned for each of the counters in the cluster, and  $E/E_{cluster}$  is the fraction  
 1400 of the total cluster energy deposited in each counter in the cluster defined in  
 1401 Eq.(21).

### 1402 *4.3 Beam Performance*

1403 The first in-beam characterization of the CTOF system took place during the  
 1404 Dec. 2017 to Feb. 2018 CLAS12 Engineering Run and subsequently during  
 1405 the first physics production running period that took place from Mar. - May  
 1406 2018. During these periods the performance of the CTOF system was tested at  
 1407 different beam energies (2.2, 6.4, 10.6 GeV), different solenoid magnetic field  
 1408 strengths and polarities (from 0 field to full field), and over a range of beam-  
 1409 target luminosities up to twice the nominal planned CLAS12 luminosity of  
 1410  $1 \times 10^{35} \text{ cm}^{-2}\text{s}^{-1}$ . In this section the measured scaler rates and PMT currents as  
 1411 a function of beam current are presented, as well as the reconstruction results  
 1412 and particle identification capabilities relative to the system specifications  
 1413 based on the current system calibrations.

#### 1414 *4.3.1 CTOF Rates and PMT Currents*

1415 The counting rates during beam operations can be viewed during data taking  
 1416 using the scalers associated with the FADCs. The threshold applied for these  
 1417 scalers are set at  $\sim 1$  MeV. During a beam current scan with a 10.6 GeV  
 1418 electron beam incident upon the 5 cm long liquid-hydrogen target from 5 nA  
 1419 to 75 nA (corresponding to the nominal design luminosity for CLAS12  $1 \times$   
 1420  $10^{35} \text{ cm}^{-2}\text{s}^{-1}$ ) the average counting rate in the different CTOF counters was  
 1421 studied. The results shown in Fig. 34 display a reasonably linear behavior.  
 1422 The rates in the downstream PMTs are roughly a factor of two larger than in  
 1423 the upstream PMTs. Part of this difference is due to the fact that the events  
 1424 seen by the CTOF are predominantly focused at the downstream end of the  
 1425 counters. Therefore the average path length for light to travel is longer to the  
 1426 upstream PMTs and the rate difference is due to the longer path length of

1427 light attenuation. However, the likely larger effect is believed to be due to  
 1428 incident radiation on the downstream light guides from splashback from the  
 1429 entrance to the beamline Møller cone and the copious conversion of  $\pi^0$  mesons  
 1430 in the region about the target. This radiation generates significant Cherenkov  
 1431 light in the light guides that is seen by the downstream PMTs and not by the  
 1432 upstream PMTs.

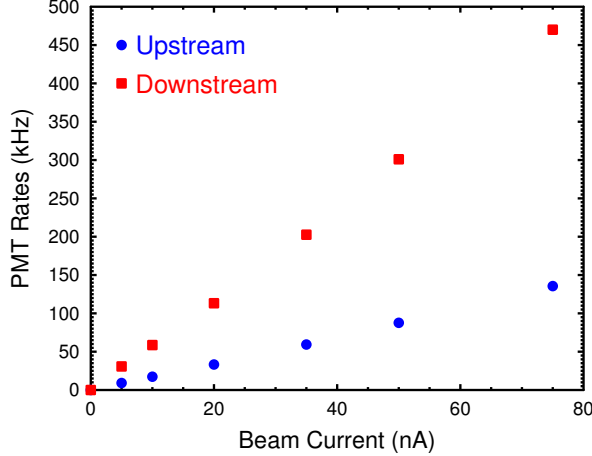


Fig. 34. (Color Online) CTOF counter rates (kHz) for 11 GeV electrons on a liquid-hydrogen target at a beam current (nA). The nominal operating luminosity of CLAS12 of  $1 \times 10^{35} \text{ cm}^{-2}\text{s}^{-1}$  corresponds to a beam current of  $\sim 75$  nA.

1433 Studies using the CLAS12 GEANT-4 Monte Carlo suite called gemc [3] at the  
 1434 full nominal luminosity indicate that the total integrated rates (hadronic and  
 1435 neutral) for particles that deposit energy greater than 1 MeV in the counters  
 1436 is  $\sim 100$  kHz/counter and the nominal PMT currents for all incident radiation  
 1437 on the counter (i.e. with no energy threshold) are  $\sim 30\text{-}40 \mu\text{A}$  [49]. Fig. 35  
 1438 shows the Monte Carlo results for the CTOF counter rates as a function of  
 1439 track momentum for different particle species.

1440 From our GEANT-4 Monte Carlo studies, the response of the CTOF with an  
 1441 11 GeV electron beam incident upon a 5 cm liquid-hydrogen target has been  
 1442 studied in detail [49]. These studies have been carried out at a beam current  
 1443 of 75 nA corresponding to the full nominal design luminosity of CLAS12 of  
 1444  $1 \times 10^{35} \text{ cm}^{-2}\text{s}^{-1}$ . The results of these studies showed that for each CTOF  
 1445 counter the incident rate of all charged and neutral particles is 4 MHz of  
 1446 which  $\sim 97\%$  is photons and leptons. With a 1 MeV energy deposition thresh-  
 1447 old in the CTOF counters to match that applied to the hardware, the rate  
 1448 of charged and neutral particles is  $\sim 130$  kHz/counter, half of which is lep-  
 1449 tons and photons and half is hadronic. Including attenuation effects along the  
 1450 scintillation bar and light guides, the measured counter rates at the PMTs  
 1451 are  $\sim 110$  kHz (upstream) and  $\sim 120$  kHz (downstream). The predictions for  
 1452 the upstream PMTs match well what is seen in direct measurements during  
 1453 beam operations. However, the predictions for the downstream PMTs are a

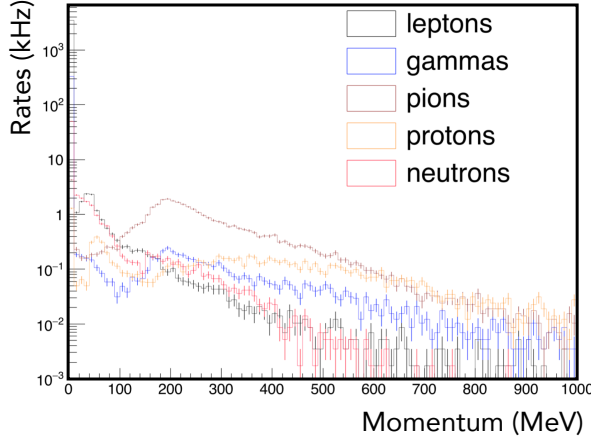


Fig. 35. (Color Online) CLAS12 Monte Carlo calculations for 11 GeV electrons on a liquid-hydrogen target at a luminosity of  $1 \times 10^{35} \text{ cm}^{-2}\text{s}^{-1}$  showing CTOF rates per counter as a function of particle momentum for leptons (black), photons (blue), charged pions (brown), protons (gold), and neutrons (red).

factor of three lower than the direct measurements. This is likely due to the fact that in the simulation the CTOF light guides are not active materials in which events that generate Cherenkov light in the light guides (see remarks above) are modeled or included.

In actuality it is not the event rate that defines the luminosity limit of the CTOF system, but the actual PMT anode currents, which are limited to  $\sim 200 \mu\text{A}$  (see Section 3.4.1). The average PMT current is directly proportional to the average number of photoelectrons  $\langle N_{phe} \rangle$  created at the photocathode by the scintillation light and the average incident charged particle event rate  $\langle R \rangle$ . This current can be expressed as:

$$\langle i_{PMT} \rangle = \langle N_{phe} \rangle \cdot Q_e \cdot G \cdot \langle R \rangle, \quad (23)$$

where  $Q_e = 1.6 \times 10^{-19} \text{ C/e}$  is the electron charge,  $G$  is the PMT gain, and  $R$  is the rate per bar. Using the expected photoelectron statistics discussed in Section 4.1.1 at a PMT gain of  $1 \times 10^6$ , the simulations estimated PMT currents of 30-40  $\mu\text{A}$  at full nominal CLAS12 luminosity. Direct measurements in beam of the PMT anode currents were made as a function of beam current as shown in Fig. 36. The measurements are about three times larger than expectations. The discrepancy is most likely due to the fact that the sampled PMT (randomly chosen on the upstream end of CTOF) was operating at a gain above  $1 \times 10^6$ .

#### 4.3.2 Reconstruction Results

Particle identification in the Central Detector of CLAS12 relies heavily on the combination of measured charged particle momenta and the flight time from

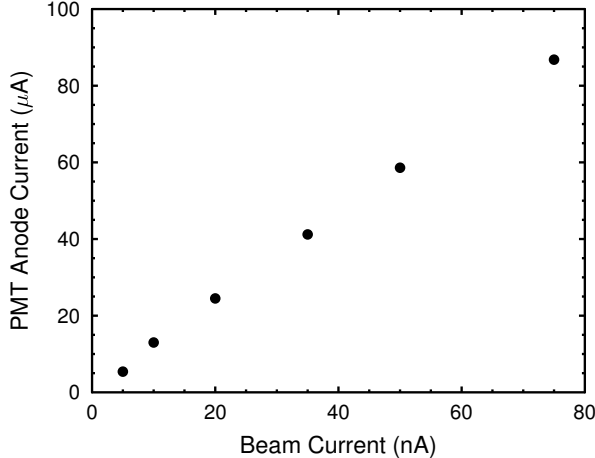


Fig. 36. Measurements of the PMT anode current ( $\mu$ A) for a representative upstream CTOF PMT as a function of beam current (nA) with a 10.6 GeV electron incident upon a 5 cm liquid-hydrogen target.

the target to the respective CTOF counters. The vertex time is determined with respect to the accelerator RF, modulo the RF period  $T_{RF}$ . The beam bucket for each event is identified using the flight time of scattered electrons or high momentum pions detected in the CLAS12 Forward Detector traced back to the interaction point. The FTOF resolution of  $< 200$  ps [5] allows clear selection of the correct beam bucket. In Fig. 37 we show the distribution of masses for all reconstructed positively and negatively charged hadrons in CTOF without any kinematic cuts other than those imposed by the detector acceptance for the data taken with a 10.6 GeV electron beam incident upon a liquid-hydrogen target and after initial calibrations of the CTOF system. A clear separation of pions and protons can be seen from these data. For these data the  $RF$  period was 4.008 ns.

Plots of velocity versus momentum are shown in Fig. 37 for positively and negatively charged particles, displaying the overall particle identification possible with this detector through the separation of the different particle species. These distributions qualitatively show the particle separation for  $\pi/K$ ,  $\pi/bnp$ , and  $K/p$  vs. momentum as required by the system specifications in Section 2 and Table 1.

## 5 Summary

We have designed and built a time-of-flight system for the CLAS12 Central Detector in Hall B at Jefferson Lab known as the Central Time-of-Flight or CTOF detector. This system consists of 48 90-cm-long scintillation bars of a wedge-shaped cross section that form a hermetic barrel at a radius of 25 cm from the beamline. As the CTOF system is positioned inside of a 5-T

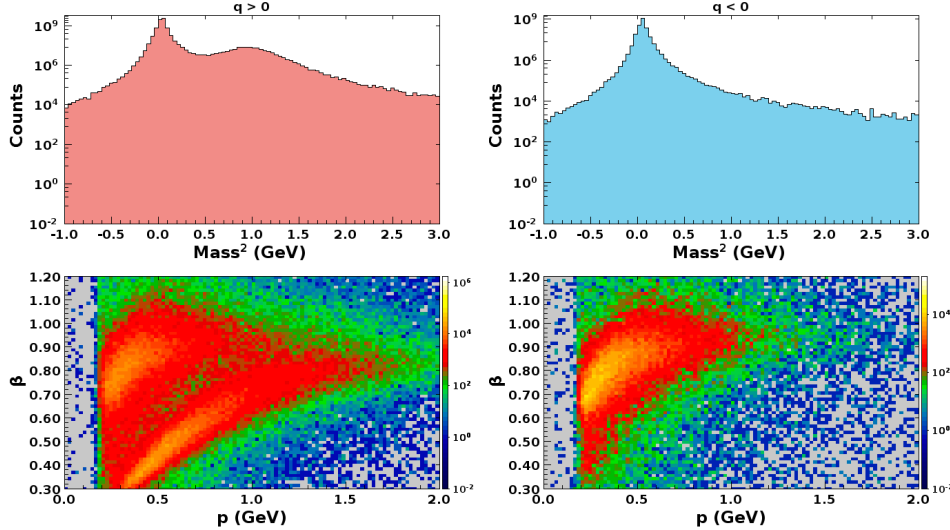


Fig. 37. (Color Online) Reconstructed mass squared ( $\text{GeV}^2$ ) and  $\beta$  vs. momentum distributions for positively charged particles (left column) and negatively charged particles (right column) for all CTOF counters from beam data with a 10.6 GeV electron incident on a liquid-hydrogen target.

superconducting solenoid, the light is delivered to the PMTs through long light guides to allow the PMTs to be positioned in reduced field regions where a multi-layer shield system reduces the magnet fringe fields to the level of 0.2 G at the PMT photocathode. The scintillation bars are read out at each end. The detector was designed to have an intrinsic time resolution of about 65 ps and this level of performance has been achieved. With these timing resolutions the CTOF system can separate  $\pi/K$  to 2.8 GeV,  $K/p$  to 4.8 GeV, and  $\pi/p$  to 5.4 GeV with  $4\sigma$  separation with up to an order of magnitude difference in the relative yields. The specifications are sufficient to meet to meet the particle identification requirements in the forward direction for the full CLAS12 physics program. The performance of the CTOF system was verified in extensive bench studies in our cosmic ray test stands as well as after installation in the first beam runs with the CLAS12 system in the period from Dec. 2017 to May 2018.

## 1515 Acknowledgements

We benefited greatly from useful discussions with and assistance from Sergey Boyarinov, Chris Cuevas, Ralf Gothe, Chris Keith, Eugene Pasyuk, Cole Smith, Elton Smith, Maurizio Ungaro, and Veronique Ziegler. We thank the Hall B technical crew for their efforts during counter installation and cabling. Finally, we thank the summer students that contributed to component assembly and testing for this system. This work was supported in part by DOE Contract #DE-AC05-84ER40150.

1523 **References**

- 1524 [1] B.A. Mecking *et al.*, Nucl. Inst. and Meth. **A503**, 513 (2003).
- 1525 [2] V.D. Burkert *et al.*, to be published in Nucl. Inst. and Meth. A, (2020).
- 1526 [3] CLAS12 GEANT4 Monte Carlo suite *gemc*, <http://gemc.jlab.org>.
- 1527 [4] E.S. Smith *et al.*, Nucl. Inst. and Meth. **A432**, 265 (1999).
- 1528 [5] D.S. Carman *et al.*, to be published in Nucl. Inst. and Meth. A, (2020).
- 1529 [6] V. Baturin *et al.*, “*Time Resolution Measurements with the Final Prototype for*  
1530 *the CLAS12 Central TOF Detector*”, CLAS-Note 2009-001.  
1531 <https://misportal.jlab.org/ul/Physics/Hall-B/clas/viewFile.cfm/2009-001.pdf?documentId=549>
- 1533 [7] V. Baturin and D.S. Carman, “*Central Time-of-Flight Geometry for CLAS12*”,  
1534 CLAS12-Note 2016-001.  
1535 <https://misportal.jlab.org/mis/physics/clas12/viewFile.cfm/2016-001.pdf?documentId=25>
- 1537 [8] Eljen Technology, 1300 W. Broadway, Sweetwater, TX 79556
- 1538 [9] Saint Gobain Crystals, 12345 Kinsman Road, Newbury, OH 44065
- 1539 [10] Eljen Technology Scintillator Polishing Guide,  
1540 [http://www.eljentechnology.com/images/technical-library/Plastic\\_Polishing.pdf](http://www.eljentechnology.com/images/technical-library/Plastic_Polishing.pdf)
- 1542 [11] Plastic-Craft Products Corporation, 744 West Nyack Rd., P.O. Box K, West  
1543 Nyack, NY 10994
- 1544 [12] F. Barbosa *et al.*, “*Status and Further Steps Towards the CLAS12 “Start”-Counter*”, CLAS-Note 2006-011.  
1545 <https://misportal.jlab.org/ul/Physics/Hall-B/clas/viewFile.cfm/2006-011.pdf?documentId=278>
- 1548 [13] G. Mutchler and Y. Sharabian, “*Wrapping Tests and Monte Carlo Evaluation of a New Highly Segmented CLAS Start Counter*”, CLAS-NOTE 2005-008.  
1549 <https://misportal.jlab.org/ul/Physics/Hall-B/clas/viewFile.cfm/2005-008.pdf?documentId=167>
- 1552 [14] 3M Optical Systems, <http://www.apioptics.com/pdf/ESR.pdf>
- 1553 [15] International Light Technologies, <http://www.intl-lighttech.com/>
- 1554 [16] Hamamatsu Corporation, 360 Foothill Rd., Box 6910, Bridgewater, NJ 08807
- 1555 [17] Hamamatsu R2083 PMT, <http://www.hamamatsu.com/us/en/R2083.html>
- 1556 [18] Hamamatsu H2431 Assembly,  
1557 <http://www.hamamatsu.com/resources/pdf/etd/PMT TPMZ0002E.pdf>

- 1558 [19] Burle Industries, 1000 New Holland Ave, Lancaster, PA 17601
- 1559 [20] H. Kichimi *et al.*, Nucl. Inst. and Meth. A **325**, 451 (1993).
- 1560 [21] V. Baturin *et al.*, Nucl. Inst. and Meth. A **562**, 327 (2006).
- 1561 [22] M. Bonesini *et al.*, Nucl. Inst. and Meth. A **567**, 200 (2006).
- 1562 [23] V. Baturin *et al.*, “*TOF Resolution Measurements with the CLAS12 Central*  
1563 *TOF Detector with Fine-Mesh Photomultiplier Tubes*”, CLAS-Note 2011-005.  
1564 <https://misportal.jlab.org/ul/Physics/Hall-B/clas/viewFile.cfm/2011-005.pdf?documentId=633>
- 1566 [24] V. Popov, Nucl. Inst. and Meth.A **505**, 316 (2003).
- 1567 [25] Opera 3-D magnetic field computations, see <http://operafea.com/>.
- 1568 [26] V. Baturin *et al.*, Nucl. Inst. and Meth. A **664**, 11 (2012).
- 1569 [27] V. Baturin and D.S. Carman, “*Design and Performance Tests of the Dynamical*  
1570 *Magnetic Shields for the CLAS12 Central Time-of-Flight Detector*”, CLAS12-  
1571 NOTE 2015-003.  
<https://misportal.jlab.org/mis/physics/clas12/viewFile.cfm/2015-003.pdf?documentId=19>
- 1574 [28] Wiener Plein and Baus Corporation,  
1575 <http://www.wiener-d.com/sc/power-supplies/mpod-lvhv/>
- 1576 [29] Poisson Superfish program,  
1577 [http://laacg.lanl.gov/laacg/services/download\\_sf.shtml](http://laacg.lanl.gov/laacg/services/download_sf.shtml)
- 1578 [30] D.S. Carman, G. Asryan, and A. Ni, “*Central Time-of-Flight Magnetic Shield*  
1579 *Performance Studies*”, CLAS12-NOTE 2015-004.  
<https://misportal.jlab.org/mis/physics/clas12/viewFile.cfm/2015-004.pdf?documentId=20>
- 1582 [31] Bicron BC-600 Optical Cement,  
1583 <http://www.crystals.saint-gobain.com/uploadedFiles/SG-Crystals/Documents/SGC%20BC600%20Data%20Sheet.pdf>
- 1585 [32] Dymax 3-20262 UV curing glue, <https://www.dymax.com/images/pdf/pds/3-20262.pdf>
- 1587 [33] VM-2002 (also called Vikuiti) Enhanced Specular Reflector,  
1588 <http://www.apioptics.com/pdf/ESR.pdf>
- 1589 [34] Dupont Tedlar Film,  
1590 <http://www.dupont.com/products-and-services/membranes-films/pvf-films/brands/tedlar-pvf-films.html>
- 1592 [35] D.S. Carman, “*Central Time-of-Flight Counter Wrapping Procedures*”,  
1593 CLAS12-Note 2016-002.  
<https://misportal.jlab.org/mis/physics/clas12/viewFile.cfm/2016-002.pdf?documentId=26>

- 1596 [36] D.S. Carman, “*Central Time-of-Flight Magnetic Shield Attachment*  
 1597 *Procedures*”, CLAS12-Note 2016-003.  
 1598 <https://misportal.jlab.org/mis/physics/clas12/viewFile.cfm/2016-003.pdf?documentId=27>
- 1600 [37] BC-630 Optical Grease,  
 1601 <https://www.crystals.saint-gobain.com/products/assembly-materials>
- 1602 [38] Ortec 935 Discriminator,  
 1603 <http://www.ortec-online.com/products/electronics/fast-timing-discriminators/935>
- 1605 [39] CAEN VX1290N TDC Manual,  
 1606 <http://www.caen.it/servlet/checkCaenManualFile?Id=12125>
- 1607 [40] E. Jastremski, <https://www.jlab.org/Hall-B/ftof/manuals/caen-inl-notes.pdf>
- 1608 [41] <https://www.jlab.org/Hall-B/ftof/manuals/FADC250UsersManual.pdf>
- 1609 [42] EPICS (Experimental Physics and Industrial Control System),  
 1610 <http://www.aps.anl.gov/epics>
- 1611 [43] D.S. Carman, “*Central Time-of-Flight System Bench Testing Results*”,  
 1612 CLAS12-Note 2016-009.  
 1613 <https://misportal.jlab.org/mis/physics/clas12/viewFile.cfm/2016-009.pdf?documentId=49>
- 1615 [44] [https://www.jlab.org/Hall-B/ctof/manuals/agilent\\_mso-x\\_manual.pdf](https://www.jlab.org/Hall-B/ctof/manuals/agilent_mso-x_manual.pdf)
- 1616 [45] D.S. Carman, “*CLAS12 CTOF Time-Walk Corrections*”, CLAS12-Note 2015-006.  
 1617 <https://misportal.jlab.org/mis/physics/clas12/viewFile.cfm/2015-006.pdf?documentId=24>
- 1620 [46] D.S. Carman, *Description of the Calibration Algorithms for the CLAS12 Central Time-of-Flight System*,  
 1621 [https://www.jlab.org/Hall-B/ctof/notes/ctof\\_calib.pdf](https://www.jlab.org/Hall-B/ctof/notes/ctof_calib.pdf)
- 1623 [47] Eljen Technologies scintillator specifications,  
 1624 [http://www.eljentechnology.com/images/technical\\_library/Physical\\_Constants\\_Plastic.pdf](http://www.eljentechnology.com/images/technical_library/Physical_Constants_Plastic.pdf)
- 1625 [48] D.S. Carman, *Central Time-of-Flight Reconstruction for CLAS12*,  
 1626 <https://www.jlab.org/Hall-B/ctof/notes/ctof-recon.pdf>
- 1627 [49] V. Burkert, D.S. Carman, L.C. Smith, and M. Ungaro, *Study of Tungsten*  
 1628 *Shielding Before CTOF to Limit its PMT Currents*, CLAS12-Note 2018-006.  
 1629 <https://misportal.jlab.org/mis/physics/clas12/viewFile.cfm/2018-006.pdf?documentId=60>